

15 **Evapotranspiration prediction for European forest sites does not improve with assimilation of**
16 **in-situ soil water content data**

17

18 L. Strebel^{1,2}, H.R. Bogaña^{1,2}, H. Vereecken^{1,2}, M. Andreasen³, S. Aranda-Barranco⁴, and H.-J.
19 Hendricks Franssen^{1,2}

20

21 Correspondence: l.strebel@fz-juelich.de

22

23 1 Agrosphere Institute, IBG-3, Forschungszentrum Jülich GmbH, Germany

24 2 Centre for High-Performance Scientific Computing in Terrestrial Systems: HPSC TerrSys, Geoverbund ABC/J, Leo-Brandt-Strasse, 52425 Jülich,
25 Germany

26 ³ Geological Survey of Denmark and Greenland, Copenhagen, Denmark

27 ⁴ Department of Ecology, University of Granada, Granada 18071, Spain

28

Form
Times
Block,
Absatz

Form
(Stand
Englis
Pt., Al

Form
(Stand
Autom
Vor:
nicht 1

Form
(Stand
Autom
Vor:
nicht 2

Form

51 *Correspondence to: Lukas Strelbel (l.strelbel@fz-juelich.de)*

52 **Abstract:**

53 Land surface models (LSM) are an important tool for advancing our knowledge of the Earth system. 54 LSM are constantly improved to represent the various terrestrial processes in more detail. High 55 quality data, freely available from various observation networks, are providing being used to improve 56 the prediction of terrestrial states and fluxes of water and energy. To optimize LSM with observations, 57 data assimilation methods and tools have been developed in the past decades. We apply the coupled 58 Community Land Model version 5 (CLM5) and Parallel Data Assimilation Framework (PDAF) 59 system (CLM5-PDAF) for thirteen forest field sites throughout Europe, covering different climate 60 zones. The goal of this study is to assimilate in-situ soil moisture measurements into CLM5 to 61 improve the modeled evapotranspiration fluxes. The modeled fluxes will be evaluated using the 62 predicted evapotranspiration fluxes with eddy covariance (EC) systems. Most of the sites use point 63 scale measurements from, however for three of the forest sites we use soil water content data from 64 cosmic-ray neutron sensors, which have a measurement scale closer to the typical land surface model 65 grid scale and EC footprint. Our results show that while data assimilation reduced the root-mean- 66 square error for soil water content on average by 56 to 64%, the root-mean-square error for the 67 evapotranspiration estimation is increased by 4%. This finding indicates that only improving the SWC 68 estimation of state-of-the-art LSM such as CLM5 still suffer from uncertainties in-is not sufficient 69 to improve evapotranspiration estimates for forest sites. To improve evapotranspiration estimates, it 70 is also necessary to consider the representation of soil hydrological processes in forests, e.g. deep root 71 LAI in magnitude and timing, as well as uncertainties in water uptake, or highly uncertain by roots 72 and vegetation parameters.

Form
12 Pt.

Form
ze

Form
Schrift

Form
12 Pt.

Form
Schrift

Form
12 Pt.

Form
Schrift

Form
12 Pt.

1. Introduction

Land surface models (LSM) are important tools to improve our understanding of the Earth system. LSM cover a broad range of land surface processes like the partitioning of incoming energy at the land surface, mass exchange between the land and atmosphere, hydrological, and ecological processes. They use sophisticated parameterizations and are constantly improved to achieve a more accurate representation of land surface processes, e.g. Arora et al. (2020) and references therein. However, there are still many sources of uncertainty introducing systematic biases in the LSM (e.g. initial conditions, atmospheric forcings, parameters, and parameterization). One approach to improve model predictions is to assimilate observational data. Improved estimates of evapotranspiration (ET) by LSM ~~is are~~ of main interest as ET is a major driver of climate ~~and~~ and weather, an important component of the water and energy cycles, closely coupled to the carbon cycle through the photosynthesis process (Jung et al., 2011). Fine spatial scale ET estimations are important to estimate water use and plant stress (Wurster et al. 2020). The flux of ET is, however, influenced by multiple factors, including soil water content, ~~(SWC)~~, soil properties, ecophysiological processes, and vegetation characteristics (Wilson et al., 2004), so it is more common to assimilate these prognostic variables rather than ET itself.

134

Many studies assimilate soil moisture products into LSMs (e.g. Hung et al., 2022; Mahmood et al., 2019; Naz et al., 2019; Liu and Mishra., 2017; Han et al., 2015) and report on the impact on hydrological variables like root-zone-moisture and runoff. Some studies use assimilation of soil water content or related variables to evaluate ET estimation of LSMs. For example, Girotto et al. (2017) assimilated terrestrial water storage from the Gravity Recovery and Climate Experiment into a land surface model and evaluated results over India. ~~However, they~~ They found that the assimilation decreased the accuracy of ET estimation compared to observations due to model limitations in representing irrigation. Peters-Lidard et al. (2011) assimilated two different remotely sensed soil water content products into the Noah land surface model over North America and found mixed results regarding the improvement of latent heat flux estimates. The domain averaged root-mean-square error of the latent heat flux reduced from 27.6 Wm^{-2} to 25.6 Wm^{-2} or increased to 29.4 Wm^{-2} depending on the assimilated soil water content product. Additionally, they show that the improvements and degradation vary spatially across their study domain, with land cover type, and as function of the season and they note that the most significant improvements occur for cropland and grassland. Liu and Mishra (2017) assimilated surface soil water content data from the Advanced Microwave Scanning Radiometer-Earth Observing System in a global Community Land Model version 4.5 and found ET bias reductions of up to 2.5mm/day compared to the Global Land Data Assimilation System (GLDAS) data product.

153

For our study, we chose the latest version (version 5) of the widely used Community Land Model (CLM5) (Lawrence et al. 2019) as various land surface process representations have been improved in CLM5 compared to earlier versions. For instance, Kennedy et al. (2019) added a plant hydraulic stress parameterization to improve the accuracy of simulated transpiration and soil water content. Lawrence et al. (2019) demonstrated the improvements of CLM5 over its precursor CLM4 in terms of ET using two study sites as examples and highlighted the better representation of the effects of soil depth on ET prediction in CLM5. On the other hand, Cheng et al. (2021) found that CLM5 predicts lower ET compared to older CLM versions and various observational data, likely due to low photosynthetic rate and leaf area index (LAI), which is consistent with their finding of low gross

208 primary production (GPP) compared to reference data in the same simulations. In addition to these
209 regional to global validation studies, CLM was used in several single point setups, i.e. simulations
210 for a single grid cell, to evaluate the performance of various LSM components. For example,
211 Hudiburg et al. (2013) used CLM 4.0 to estimate net primary production (NPP) and GPP of a forested
212 site and compared it with eddy covariance (EC) measurements. Another study (Zhang et al., 2019)
213 reduced an overestimation of growing-season LAI and annual GPP of a grassland site for a CLM 4.5
214 single-point setup. More recently, CLM5 was extended to consider both cover crop management with
215 improvements to ET estimation of up to 57% (Boas et al., 2021) and fruit tree cultivation using
216 extensive field measurements with high correlation between observed and modeled ET (Dombrowski
217 et al., 2022). Other studies have used manual tuning of parameters to improve CLM simulations for
218 forests. For instance, Duarte et al. (2017) calibrated CLM4.5 for an old-growth coniferous forest and
219 found good agreement between simulated and observed response of canopy conductance to
220 atmospheric vapor pressure deficit and soil water content. Racza et al. (2016) used CLM4.5 and
221 implemented a seasonally varying calibration of vegetation parameters and accurately simulated net
222 carbon exchange, latent heat exchange, and biomass.

223
224 In this study, we investigate if assimilating high quality, in-situ soil water content measurements can
225 improve the evapotranspiration estimates of LSM. We focus on one specific land cover type, namely
226 forests. In a previous study (Strebel et al. 2022), we investigated the potential for data assimilation of
227 in-situ SWC measurements to improve model estimation for a single forest site. This study expands
228 this method to more forest sites and investigates the effect of improved SWC estimation on ET. To
229 investigate this, we use point and plot scale in-situ soil water content measurements. For most sites
230 we use point measurements provided by FLUXNET (Balocchi et al., 2020) and eLTER Europe. The
231 FLUXNET data have been used in various studies to verify or compare model results. For example,
232 Dirmeyer et al. (2018) used FLUXNET data to compare four model systems, including CLM4.5, in
233 three configurations and found for annual averaged ET that correlations range from 0.28 to 0.43 and
234 for sensible heat from 0.14 to 0.54. The point scale measurements use invasive equipment and the
235 specific measurement volume, exact depth of the sensors, number of sensors, and number of stations
236 varies from site to site. For a few sites we use soil water content measurements from Cosmic Ray
237 Neutron Sensing (CRNS) from the COSMOS-Europe data set (Bogena et al., 2022). The CRNS
238 provides continuous and non-invasive soil water content measurements over a spatial footprint of
239 hundreds-of-meters and integrates from the surface to a depth of 10-70 cm vertically in the soil (Zreda
240 et al., 2008; Köhli et al., 2015). CRNS use neutrons as proxy for SWC and the vertical measurement
241 depth varies with the soil moisture conditions. Additionally, the uncertainty of CRNS-derived soil
242 moisture varies not only with the different neutron detectors but also with the number of counts in a
243 time period and therefore results under lower soil moisture conditions are more accurate (Bogena et
244 al., 2022). The spatial footprint area is similar to the footprint of the EC flux tower. We use the final
245 processed data on soil water content and vertical penetration (measurement) depth provided by the
246 COSMOS-Europe dataset (Bogena and Ney, 2021). In this study, we use the ensemble Kalman filter
247 to assimilate in-situ soil water content measurements into CLM5 simulations and the effect on the
248 modeling results are quantified by comparing the modeled ET against the observed ET obtained from
249 EC flux towers. We also analyze the effects on other land-atmosphere exchange fluxes, i.e. net
250 ecosystem exchange (NEE) and gross primary production (GPP). The paper is structured as follows:
251 First, we introduce the model and data assimilation framework used. The sites selected for this study
252 and the observational data used for data assimilation and model-observation comparison are then

256 described. Subsequently, the results for each variable of interest are shown and analyzed. Finally, we
257 end with a discussion of the obtained results and conclusions.
258

Form
12 Pt.

275 **2. Methods and Materials**276 **2.1 Study sites**

277

278 In our study, we are interested in the characterization of water, energy and carbon exchange between
279 (European) forest ecosystems and the atmosphere, and whether soil water content assimilation can
280 improve the characterization of these processes. Therefore, we selected European sites with different
281 forest types (see Table 1) covering different climate zones in Europe. Another important constraint
282 was the availability of soil water content data and evapotranspiration measurements for the period
283 from 2009 to 2018. The selected sites are mostly part of FLUXNET (Balocchi et al., 2020) or the
284 European Long-Term Ecological Research network (eLTER-Europe) (Parr et al., 2002). In addition
285 to the sites from these observation networks, we included three sites from the COSMOS-Europe
286 network (Bogena et al., 2022) where cosmic-ray neutron sensors (CRNSs) are installed to estimate
287 the soil water content of the forested sites. Table 1 gives an overview of all selected sites for this
288 study and Figure 1 shows the distribution on the map.

Form

Form

12 Pt.

Form

Form

Schrift

Form

1.15 z.

Form

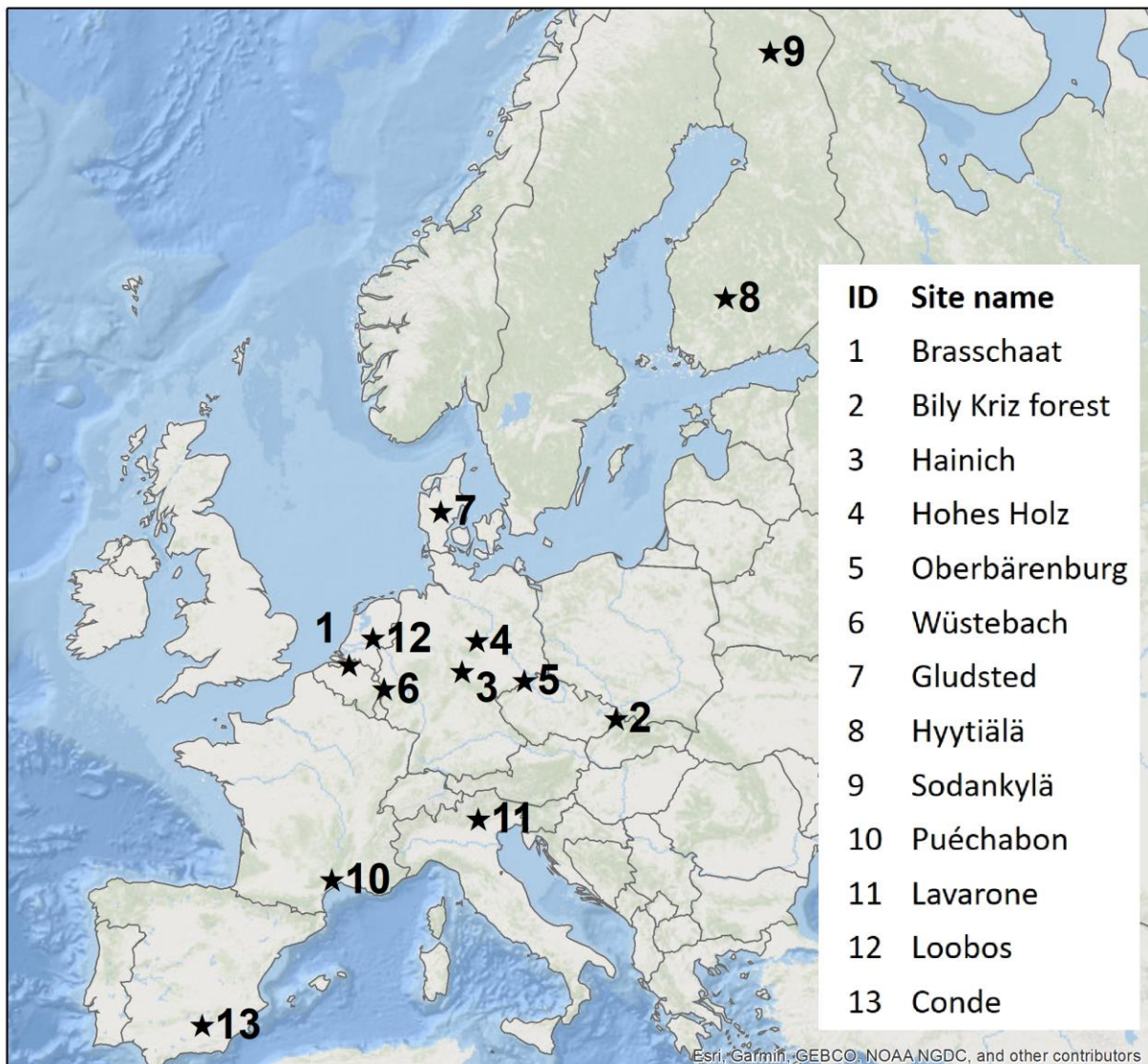
12 Pt.

Form

Schrift

Form

12 Pt.



301

302 **Figure 1: Map showing the location of the selected study sites of the FLUXNET, eLTER and COSMOS**
303 **Europe networks.**

304

In this study, daily average soil water content data are assimilated (see section 2.4.1 for more details) and the model is verified using daily average evapotranspiration and sensible heat flux data. Since the observational data were already quality controlled by the providers, we did not filter out any data. Additionally, gaps in We only assimilated (daily mean averaged) soil water content observations were not filled and only soil water content data were assimilated for days when observations measurements were available for a given day. The daily mean averages were calculated independent from the observation frequency for the different sites. Similarly, simulated evapotranspiration was only compared with observations when data were available, on the basis of daily mean averages.

Form Schrift

Form Schrift

Form

Form Schrift

350 **2.2 Model description**

351 For our study, we used the Community Land Model version 5.0 (CLM5) that can be applied in various
352 configurations (Lawrence et al. 2019). We use CLM5-BGC, i.e. CLM5 with the biogeochemistry
353 module active as opposed to CLM5 with fixed phenology. The biogeochemistry module enables a
354 fully prognostic treatment for carbon and nitrogen in the land surface model and has a significant
355 impact on the modeled water and energy budgets.

CLM5 uses a sub-grid hierarchy of various Plant Functional Types (PFTs) to characterize the land-use and vegetation type within every grid cell, e.g. evergreen needle leaf or deciduous broad leaf forests. CLM5 contains a spatially variable soil depth with an underlying, impermeable bedrock instead of the unconfined aquifer parameterization used in the former CLM4 versions. To estimate the soil water content, CLM5 solves the Richard's equation using the Brooks-Corey parameters derived from pedotransfer functions from Clapp and Hornberger (1978) with a finite-difference approximation to represent the vertical discretization and temporal evolution of soil water content. The sensible and latent heat flux estimation in CLM5 is derived from the Monin-Obukhov Similarity Theory and differentiated for vegetated and non-vegetated surfaces. ~~We only study forested areas where CLM5 partitions the simulates~~ sensible ~~heat~~ and latent heat flux ~~into vegetation for both vegetated and ground fluxes. For the vegetation part the contributions from the leaf boundary layer, the sunlit and shaded stomatal resistances affect the total resistance to the modeled water vapor transfer. The water vapor transfer includes transpiration from dry leaf surfaces and the transpiration removes water from the soil based on root fraction for a given soil layer. Interception, throughfall and canopy drip are explicitly modeled in CLM5 and canopy evaporation is partitioned represented as from the sum of stem and leaf surface evaporation based on the vegetation as a function of temperature. The ground fluxes, e.g. from bare soils or soil beneath a canopy, are dependent on the ground surface temperature. The ground latent heat flux is reduced if not enough soil moisture is available and the excess energy is redistributed to the sensible heat flux. The detailed procedure and equations are documented in Lawrence et al. (2018).~~

378 2.3 Data assimilation

379 2.3.1 Ensemble Kalman filter

380 In this work, assimilation of soil water content measurements is performed with the Ensemble Kalman
 381 Filter (EnKF) (Evensen, 1994; Burgers et al., 1998). The EnKF uses an ensemble modeling approach,
 382 with various simultaneous model runs, to approximate the model uncertainty. The ensemble members
 383 have different input model parameters and atmospheric forcings (see section 2.4 for details). We
 384 define a state vector x and an observation vector y , e.g.

417
$$\mathbf{x}^i = \begin{pmatrix} \theta_{1,1}^i \\ \theta_{1,2}^i \\ \vdots \\ \theta_{1,m}^i \\ \vdots \\ \theta_{n,m}^i \end{pmatrix} \quad (1)$$

418
$$\mathbf{x}^i = \begin{pmatrix} \theta_{1,1}^i \\ \theta_{1,2}^i \\ \vdots \\ \theta_{1,m}^i \\ \vdots \\ \theta_{n,m}^i \end{pmatrix} \quad (1)$$

419 where n is the number of layers and m is the number of grid cells, $\theta_{j,l}^i$ is the soil water content for
 420 layer j and grid cell l of the model and the superscript i refers to ensemble member i. In this study we
 421 use an ensemble of 96 member to sample the model uncertainty.

422
$$\mathbf{y} = \mathbf{o} + \mathbf{e}$$

423
$$\mathbf{y} = \mathbf{o} + \mathbf{e} \quad (2)$$

424 where o is a vector of the observational data and e represents a perturbation vector with mean zero
 425 and covariance according to the observational error covariance matrix. This perturbation vector is
 426 used to correct the error statistics as described in Burgers et al. (1998).

427 The update step of the ensemble Kalman filter is:

428
$$\mathbf{x}_a^i = \mathbf{x}_f^i + \mathbf{K}[\mathbf{y} - \mathbf{H}\mathbf{x}_f^i] \quad (3)$$

429
$$\mathbf{x}_a^i = \mathbf{x}_f^i + \mathbf{K}[\mathbf{y} - \mathbf{H}\mathbf{x}_f^i] \quad (3)$$

430 where the superscript i refers to ensemble member i, \mathbf{x}_a^i is the updated state vector after the analysis,
 431 \mathbf{x}_f^i is the forecasted model state vector, K is the Kalman gain and H is the measurement operator
 432 that transforms between model and observational states. In this study, the measurement operator H
 433 consists of a simple mapping of the observations to the corresponding model layers in the state vector
 434 for simulations with point measurements. For FLUXNET sites, measured soil water content is
 435 provided for up to three depths described as superficial, medium, and deep. Since data assimilation
 436 in CLM5-PDAF requires a specific vertical layer, we assigned 5, 20 and 50 cm to the respective
 437 FLUXNET SWC layers. For the CRNS sites, the measurement depth for each individual
 438 measurement is calculated following Schrön et al. (2017) and is included in the dataset from Bogena
 439 et al. (2022). For simulations assimilating CRNS, H assigns the mean observed SWC to all the layers
 440 down to the measurement depth. This is a simplified approach and will be improved in further studies
 441 to take the weighting function from Schrön et al. (2017) into account. The Kalman gain is calculated
 442 accordingly:

443
$$\mathbf{K} = \mathbf{P} \mathbf{H}^T (\mathbf{R} + \mathbf{H} \mathbf{P} \mathbf{H}^T)^{-1} \quad K = \mathbf{P} \mathbf{H}^T (\mathbf{R} + \mathbf{H} \mathbf{P} \mathbf{H}^T)^{-1} \quad (4)$$

444 where the superscript T is used for transposed matrices, R is the observational error covariance matrix,
 445 and P is the model error covariance matrix, which is approximated through ensemble statistics,
 446 specifically:

447
$$\mathbf{P} \mathbf{P} = \frac{1}{(N-1)} \sum_{i=1}^N (\mathbf{x}_f^i - \bar{\mathbf{x}}_f)(\mathbf{x}_f^i - \bar{\mathbf{x}}_f)^T \sum_{i=1}^N (\mathbf{x}_f^i - \bar{\mathbf{x}}_f)(\mathbf{x}_f^i - \bar{\mathbf{x}}_f)^T \quad (5)$$

448 where N is the number of ensemble members and $\bar{\mathbf{x}}$ is the ensemble mean.

482 In this study, the state vector depends on the simulation scenario (explained in more detail in section 483 2.3.2) and R is based on the measurement errors which are assumed to be constant and independent 484 with a root-mean square error of $0.02 \text{ cm}^3/\text{cm}^3$.

485 To enable data assimilation with CLM5, we use the Parallel Data Assimilation framework (PDAF) 486 (Nerger et al. 2005), which was recently coupled to CLM5 (Strebel et al. 2022). This coupling 487 (CLM5-PDAF) also supports the assimilation of soil water content measurements.

488 2.3.2 Parameter updating

489 In addition to the use of data assimilation for state updating, we also perform parameter updating 490 based on the state augmentation approach (Friedland, 1969; Fertig et al., 2009). Here, model 491 parameters are attached to the state vector and updated based on the Kalman gain calculations without 492 observations of the model parameters. By default, CLM5-PDAF updates soil hydraulic parameters 493 through changes to fractions of sand, clay, and organic matter and the pedotransfer function of Clapp 494 and Hornberger (1978). In this indirect approach the state vector for the EnKF is defined as follows:

$$496 \mathbf{x}^i = \begin{pmatrix} \theta^i \\ \%sand^i \\ \%clay^i \\ \%organic^i \end{pmatrix} \quad (6)$$

$$497 \mathbf{x}^i = \begin{pmatrix} \theta^i \\ \%sand^i \\ \%clay^i \\ \%organic^i \end{pmatrix} \quad (6)$$

498 where the superscript i refers to ensemble member i . The components θ , %sand, %clay, 499 and %organic each represent a vector containing the respective variable for each soil layer of each 500 grid cell of the model. A damping factor of 0.1 is used on the parameter updates to avoid filter 501 inbreeding and keep the ensemble spread larger so that the model error covariance matrix is a good 502 approximation for model uncertainty.

503

504 In previous studies parameters were updated indirectly (Naz et al., 2019; Han et al., 2014; Baatz et 505 al., 2017). We tested directly updating saturated hydraulic conductivity, porosity, hydraulic 506 conductivity exponent, and soil matric potential but this resulted in more unstable estimates than 507 indirectly updating soil hydraulic parameters. The pedotransfer function which is used for the indirect 508 updating results in reasonably correlated soil hydraulic parameters. “In testing a direct approach to 509 updating saturated hydraulic conductivity, porosity, hydraulic conductivity exponent B, and soil 510 matric potential we found that updating the parameters indirectly to provide more stable simulations. 511 The pedotransfer function keeps the soil hydraulic parameters reasonably correlated to each other. In 512 this study, the parameters are chosen to optimize the SWC estimation and not ET estimation to study 513 the effects of SWC improvements on ET. To more directly improve the ET estimation, parameters 514 affecting the ET process directly should be added, e.g. vegetation hydraulic parameters.

551 2.4 Model setup

552 2.4.1 Domain setup

553 Since we only use local field measurements, we represent each study site as a single grid cell in CLM5. 554 This approach is also consistent from the viewpoint of larger regional scale models, where each of 555 these sites would only be part of a grid cell. The CLM5 grid cells are vertically divided into 25 layers 556 from the surface down to 50 m depth of which the first 20 layers (until 8.6 m depth) may be 557 hydrologically and biogeochemically active depending on the variable soil depth for each site 558 (Lawrence et al., 2018). For the more than 70 different surface parameters of CLM5, we used the 559 default values generated by the tools provided with CLM5 (e.g. soil depth to bedrock, sand, clay, and 560 organic matter fractions, PFTs). These default values are generated from remapping various global 561 files (Lawrence et al., 2019). Only the PFT were manually assigned for each site. For the ensemble 562 creation, the fractions of sand, clay, and organic matter are modified for each ensemble member. The 563 perturbations are normally distributed with mean zero and a standard deviation of 10%. ~~For~~ 564 ~~FLUXNET sites, measured soil water content is provided for up to three depths described as~~ 565 ~~superficial, medium, and deep. Since data assimilation in CLM5 PDAF requires a specific vertical~~ 566 ~~layer, we assigned 5, 20 and 50 cm to the respective FLUXNET SWC layers. For the CRNS sites, the~~ 567 ~~measurement depth for each individual measurement is calculated following Schrön et al. (2017) and~~ 568 ~~is included in the dataset from Bogena et al. (2022).~~

569 2.4.2 Atmospheric forcings

570 Meteorological observations were also available at the selected study sites and were used to force
 571 CLM5. The existing gaps in the observation time series were gap-filled with data from the COSMO-
 572 REA6 reanalysis data product (Bollmeyer et al., 2015). For the ensemble generation precipitation
 573 (PR), shortwave radiation (SW), longwave radiation (LW), and air temperature (TA) were perturbed
 574 taking into account cross-correlations between variables according Reichle et al. (2007). The
 575 perturbations are: multiplicative PR ~ logN(1, 0.5), multiplicative SW ~ logN(1, 0.3), additive LW ~
 576 N(0, 20) (W/m²), and additive TA ~ N(0, 1) (°K). The following cross-correlation coefficients
 577 between variables were used: PR-SW -0.8, PR-LW 0.5, PR-TA 0, SW-LW -0.5, SW-TA 0.4 and
 578 LW-TA 0.4..

579 2.4.3 Data assimilation experimental setups

580 Three different simulation scenarios were considered: 1) Open loop (OL) simulations without data assimilation; 581 2) Data assimilation with updating of soil water content (DAS); and 3) Data assimilation with soil water content updating and parameter updating (DASP). For all scenarios data assimilation 582 is performed at a daily frequency and with daily averages from the observations. ~~For DASP a damping 583 factor of 0.1 is used on the parameter updates to avoid filter inbreeding and keep the ensemble 584 spread larger so that the model error covariance matrix is a good approximation for model 585 uncertainty.~~ The observation error is assumed to be constant and set to a RMS of 2%. .

2.5 Statistical metrics

For the comparison of simulation results with observations, we use four statistical metrics: the squared correlation coefficient (R^2), the mean bias error (MBE), the root-mean-square error (RMSE), and the unbiased root-mean-square-error (ubRMSE):

$$R^2 = 1 - \frac{\sum_{t=1}^N (o_t - m_t)^2}{\sum_{t=1}^N (o_t - \bar{o})^2} \quad (7)$$

$$MBE = \frac{\sum_{t=1}^{Nt} (m^t - o^t)}{Nt} \quad (8)$$

$$RMSE = \sqrt{\frac{\sum_{t=1}^{Nt} (m^t - o^t)^2}{Nt}} \quad (9)$$

$$\text{ubRMSE} = \sqrt{\frac{\sum_{t=1}^{Nt} [(m^t - \bar{m}^t) - (o^t - \bar{o}^t)]^2}{Nt}} \quad (10)$$

$$R^2 = 1 - \frac{\sum_{t=1}^{Nt} (o^t - m^t)^2}{\sum_{t=1}^N (o^t - \bar{o}^t)^2} \quad (7)$$

$$MBE = \frac{\sum_{t=1}^{Nt} (m^t - o^t)}{Nt} \quad (8)$$

$$RMSE = \sqrt{\frac{\sum_{t=1}^{Nt} (m^t - o^t)^2}{Nt}} \quad (9)$$

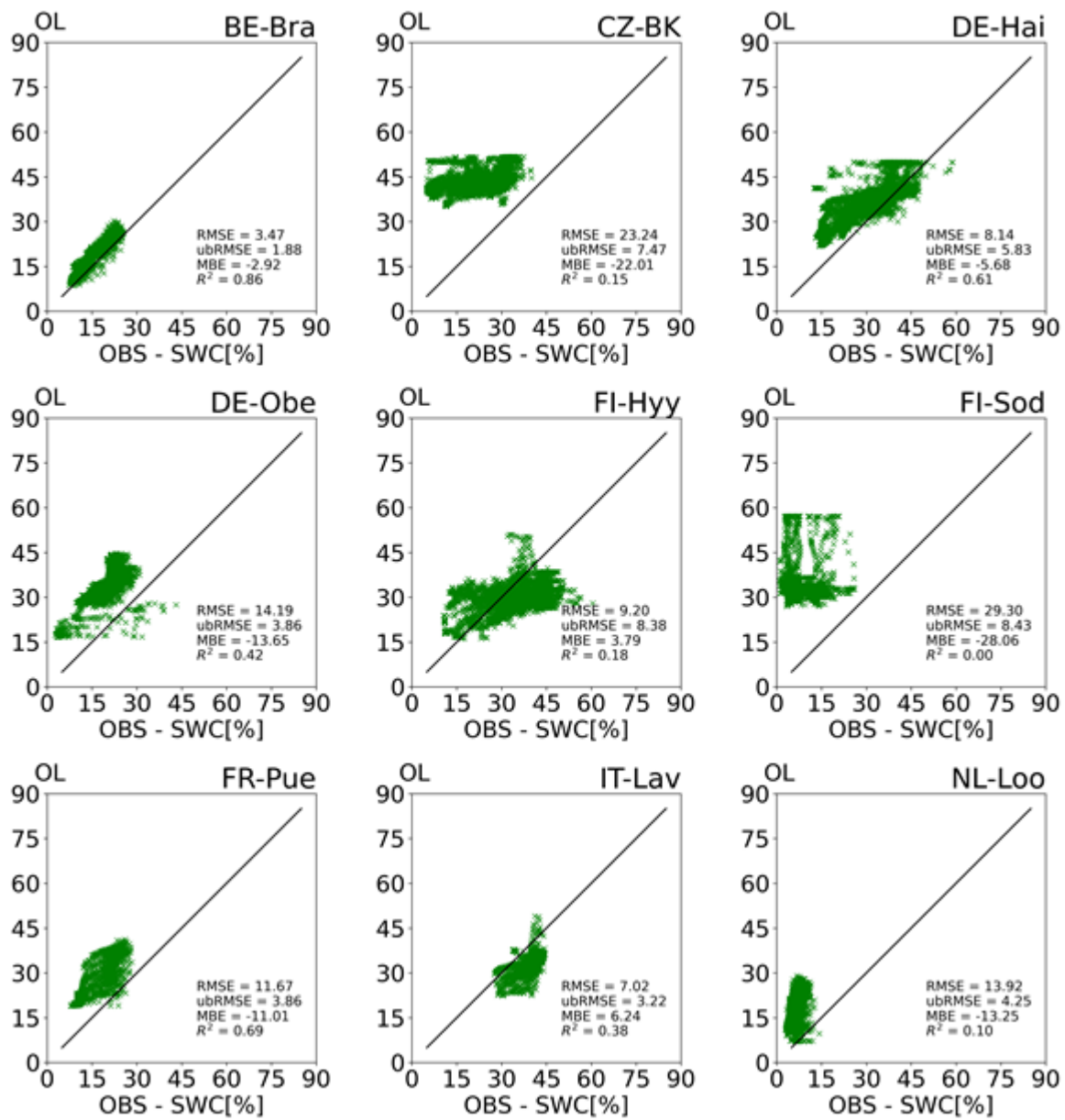
$$ubRMSE = \sqrt{\frac{\sum_{t=1}^{Nt} [(m^t - \overline{m^t}) - (o^t - \overline{o^t})]^2}{Nt}} \quad (10)$$

where \mathbf{o} stands for observations, \mathbf{m} represents the ensemble average of the simulated values, t is the time step, N_t the total number of time steps and overbar represents the average over all time steps.

3. Results

3.1 Soil water content and related parameters

Figures 2, 3 and 43 show the results of the soil water content simulations at 20 cm depth of the OL, DAS and DASP simulations compared to the soil water content observed at the nine sites. Figure 2 compares the OL and DAS results and Fig. 3 compares the OL and DASP results. The corresponding scatter diagrams for the depths 5, 20, and 50 cm can be found in the appendix (Figures A1, A2, A3, and A4 - A7). Overall, the results show expected improvements by data assimilation of observed soil water content. For the OL simulations, Fig. 2 shows particularly large RMSE values for CZ-BK, DE-Obe, FI-Sod and NL-Loo. Fig. 32 also illustrates the improved performance achieved by DASP, with a RMSE reduction from $29.3 \text{ cm}^3/\text{cm}^3$ to $6.25 \text{ cm}^3/\text{cm}^3$ and a MBE reduction from $28.06 \text{ cm}^3/\text{cm}^3$ to $-2.94 \text{ cm}^3/\text{cm}^3$ for FI-Sod. Parameter updating, as shown in Fig. 43, further improves the simulation results, but the improvement from DAS to DASP is significantly less than from OL to DAS.

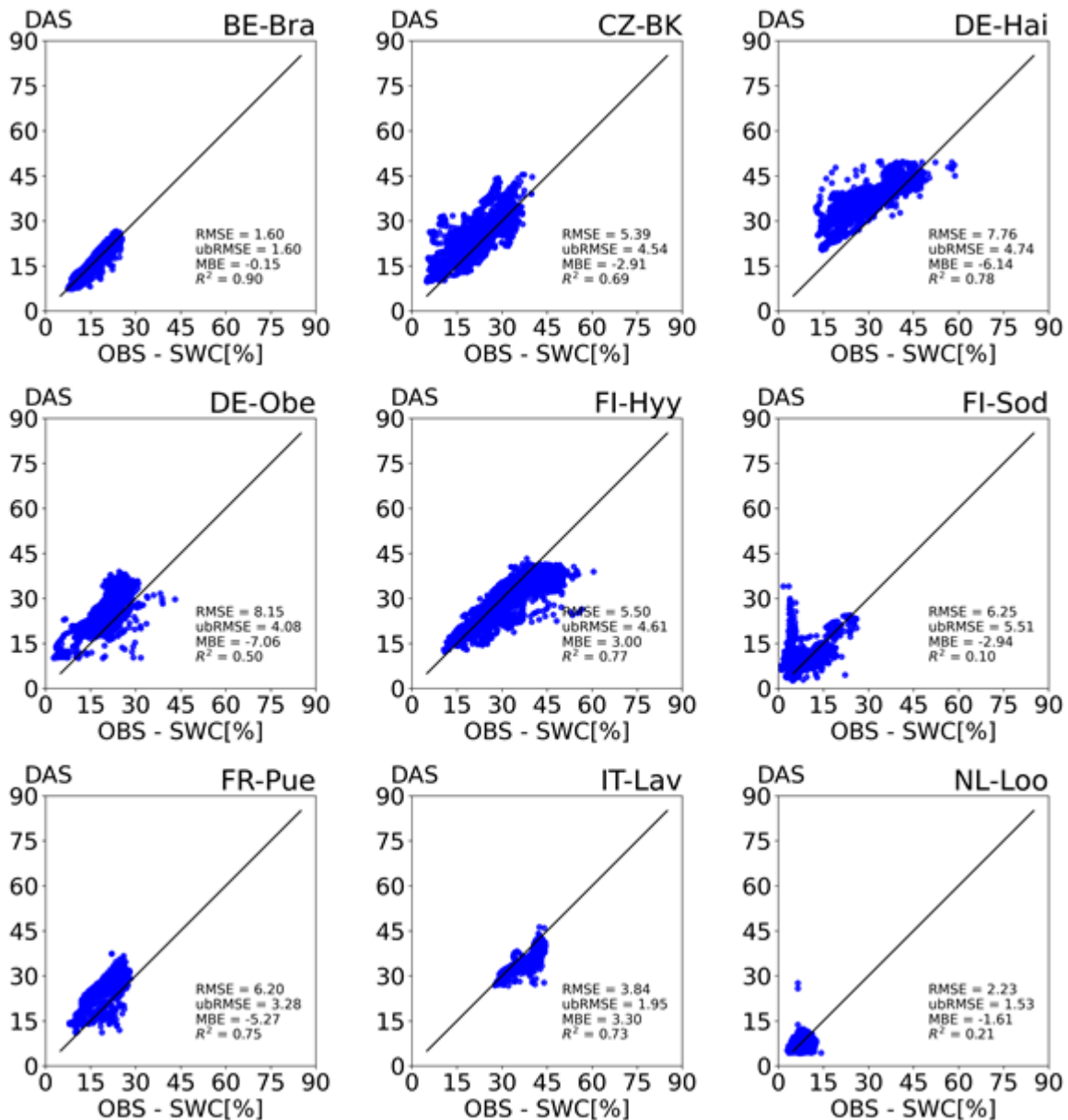


643

644

645

Figure 2: Scatter plots of observed soil water content at nine study sites versus OL simulation results at 20 cm depth. The points represent daily averages for the days observation data are available.



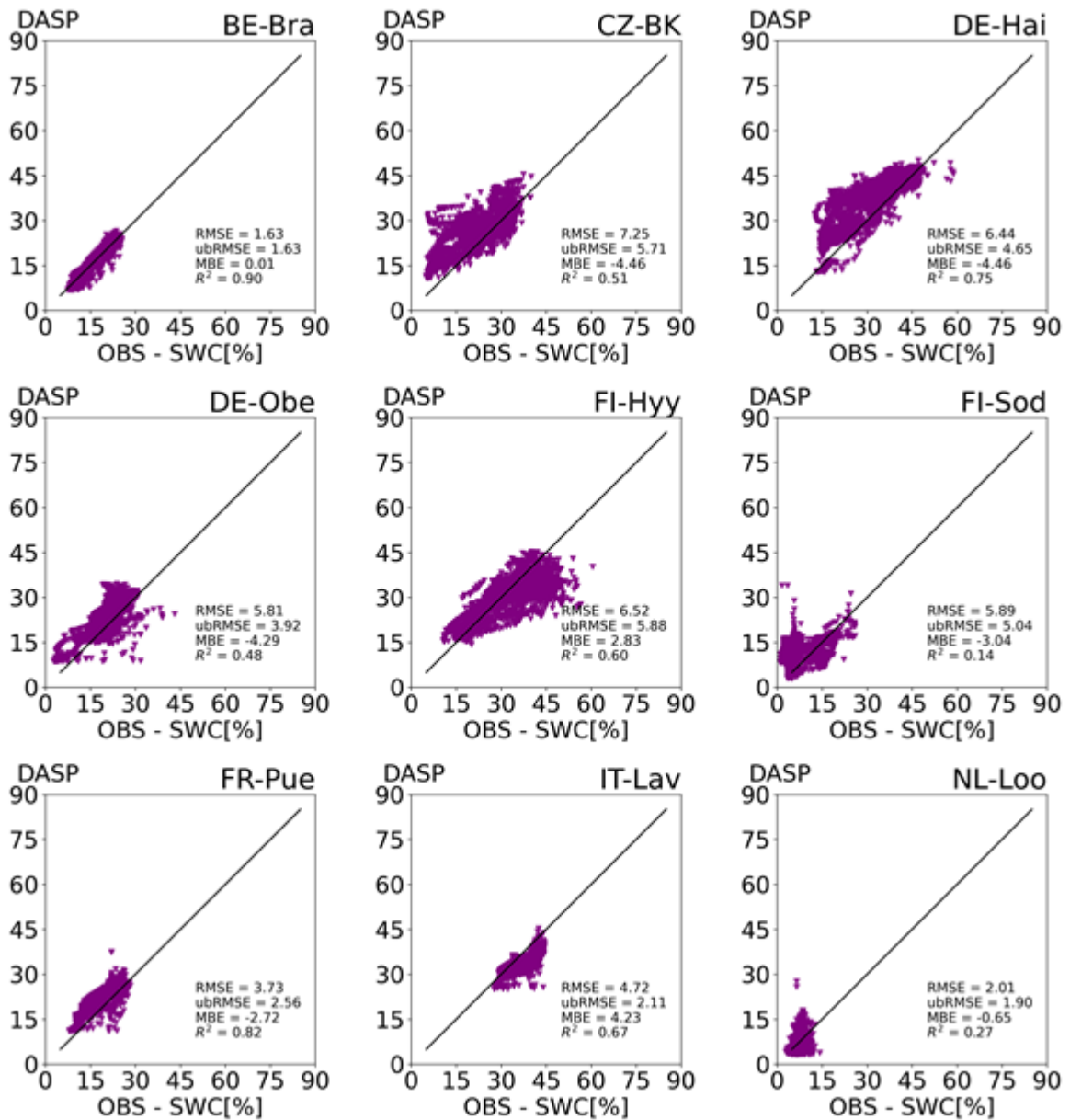
646

647

648

649

Figure 3: Scatter plots of observed soil water content at nine study sites versus DAS simulation results at 20 cm depth. The points represent daily averages for the days observation data are available.



659

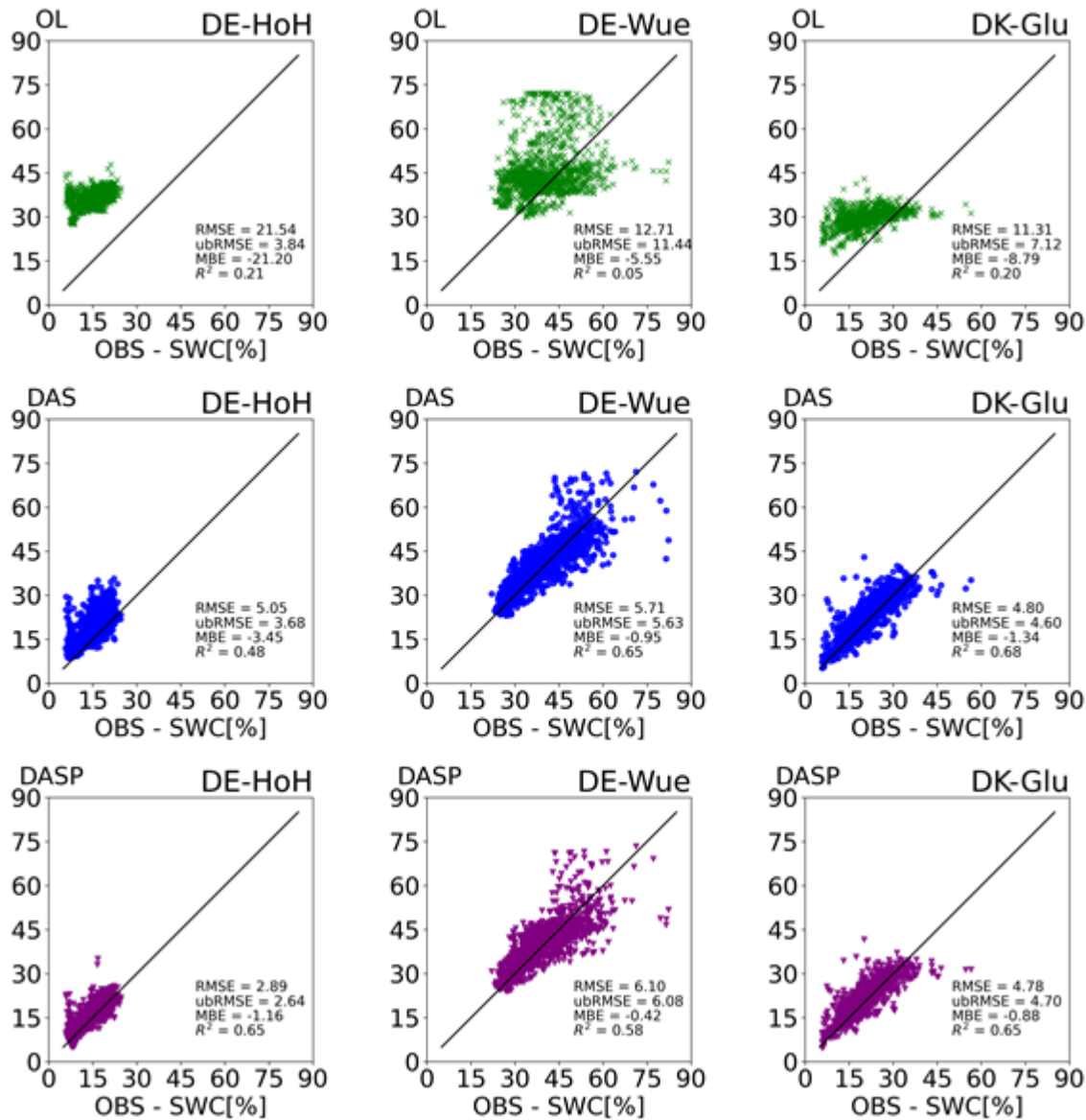
660 **Figure 4: Scatter plots of observed soil water content at nine study sites versus DASP simulation**
 661 **results at 20 cm depth. The points represent daily averages for the days on which observation data**
 662 **are available.**

663

664 The results of the three COSMOS-Europe sites are shown in Figure 54, in which the observed SWC
 665 values are compared with the weighted SWC mean of the model layers corresponding to the
 666 measurement depth of CRNS. This comparison again shows the large improvement from OL to DAS,
 667 and a smaller improvement or even a small deterioration from DAS to DASP.

Form

Form
SchrifForm
12 Pt.Form
SchrifForm
SchrifForm
SchrifForm
12 Pt.



681

682 **Figure 5** shows time series of the estimated saturated soil hydraulic conductivity for each of
 683 the sites and the three observation layer depths. The DASP scenario results in parameter changes
 684 when the first observations are available but converge over the time of the simulation to a new value.
 685 The corresponding time series for the other soil hydraulic parameters can be found in the appendix
 686 (Figures A8, A9, and A10). The sand, clay, and organic matter fraction and thus the soil hydraulic
 687 parameters can vary with depth but as shown in Fig. 5 the DA updates to the parameters affect the
 688 different layers similarly.

689 ~~Scatter plots of observed soil water content at three CRNS study sites (DE-HoH left column, DE-Wue middle column, DK-Glu right column) versus simulation results (OL results in the top row, DAS results in the middle row, and DASP results in the bottom row). The points represent daily averages for the days on which observation data are available.~~

Form
Nicht
Form
Pt., Ze
Form
Schrift
Form
12 Pt.
Form
Schrift

729 **3.2 Evapotranspiration**

730 The impact of the data assimilation on the ET flux is shown in Figures 6 and 7. Notably, the difference
731 between the OL and the DASP results is smaller for ET than for SWC. While the data assimilation
732 improves the model results for SWC for all sites, both improvement and deterioration occur for
733 modeled ET. Figure 8 shows the comparison of the improvements by data assimilation for SWC and
734 the positive and negative effect on ET estimation. The average RMSE reduction for the DASP SWC
735 prediction is between 56% and 64% compared to OL. Comparing the OL and DASP results for ET
736 shows an average reduction of the MBE of 0.06 mm/day, but an increase in RMSE for the DASP ET
737 predictions of 4 % on average, with 8 of the 13 sites showing a relative change in ET of only +/- 1 %.
738 Two outliers (FI-Sod and NL-Loo sites) reduce the average model improvement ~~in particular~~. These
739 sites show both a large overestimation in SWC in the OL (see Fig. 2) and a large underestimation of
740 ET in the DASP simulation (see Fig. 7). This ~~indicates that could be caused by~~ the SWC-ET relation
741 ~~is incorrect mismatch of simulated and actual LAI~~ for these sites. ~~A~~ To investigate this, we repeated
742 the simulations using CLM5 with satellite-derived phenology (CLM5-SP) the results are shown in
743 Fig. 9. For CLM5-SP we observe an average improvement in the RMSE of SWC between 57.6 %
744 and 64.3 % and an average reduction of 5.8 % for the ET estimation. These CLM5-SP simulations
745 use the default datasets from CLM5 and without site specific calibration of the timing or magnitude
746 of the seasonal phenology of LAI. Therefore, even for the CLM5-SP simulations there is a mismatch
747 between simulated and actual LAI. However, also for this case there are sites with large improvement
748 in SWC estimation that show deterioration for ET estimation.

749 Another possible explanation ~~for the improvement in SWC estimation but no improvement of ET~~
750 ~~estimation is the underestimation of root~~ water uptake ~~by roots in the from~~ deeper soil layers ~~is~~
751 ~~underestimated~~ for forest sites, as also suggested by Shrestha et al. (2018). Fig. 8 shows that the
752 quality of the model results is not dependent on the forest type, i.e. the evergreen needle leaf forests
753 (ENF) sites show both strong and average relative changes in SWC RMSE and ET RMSE. This
754 suggests that the strong deviations ~~in~~ the model results of the FI-Sod and NL-Loo sites are due to
755 other local conditions, e.g. soil properties.

756

757 The three CRNS sites show an average relative change of ET RMSE of -2.6%, -0.2%, and -0.9% for
758 DE-HoH, DE-Wue, and DK-Glu, respectively. Therefore, although the CNRS measurements are
759 more consistent with the large measurement area of the flux towers, no significant improvement in
760 ET for these three sites can be achieved with the current implementation of the CNRS-SWC
761 assimilation. We anticipate that the implementation of a more accurate observation operator would
762 improve the modeled SWC. The current observation operator does not use vertical weighting to take
763 the decreasing CRNS sensitivity with depth into account.

Form
Schrift

Form
12 Pt.

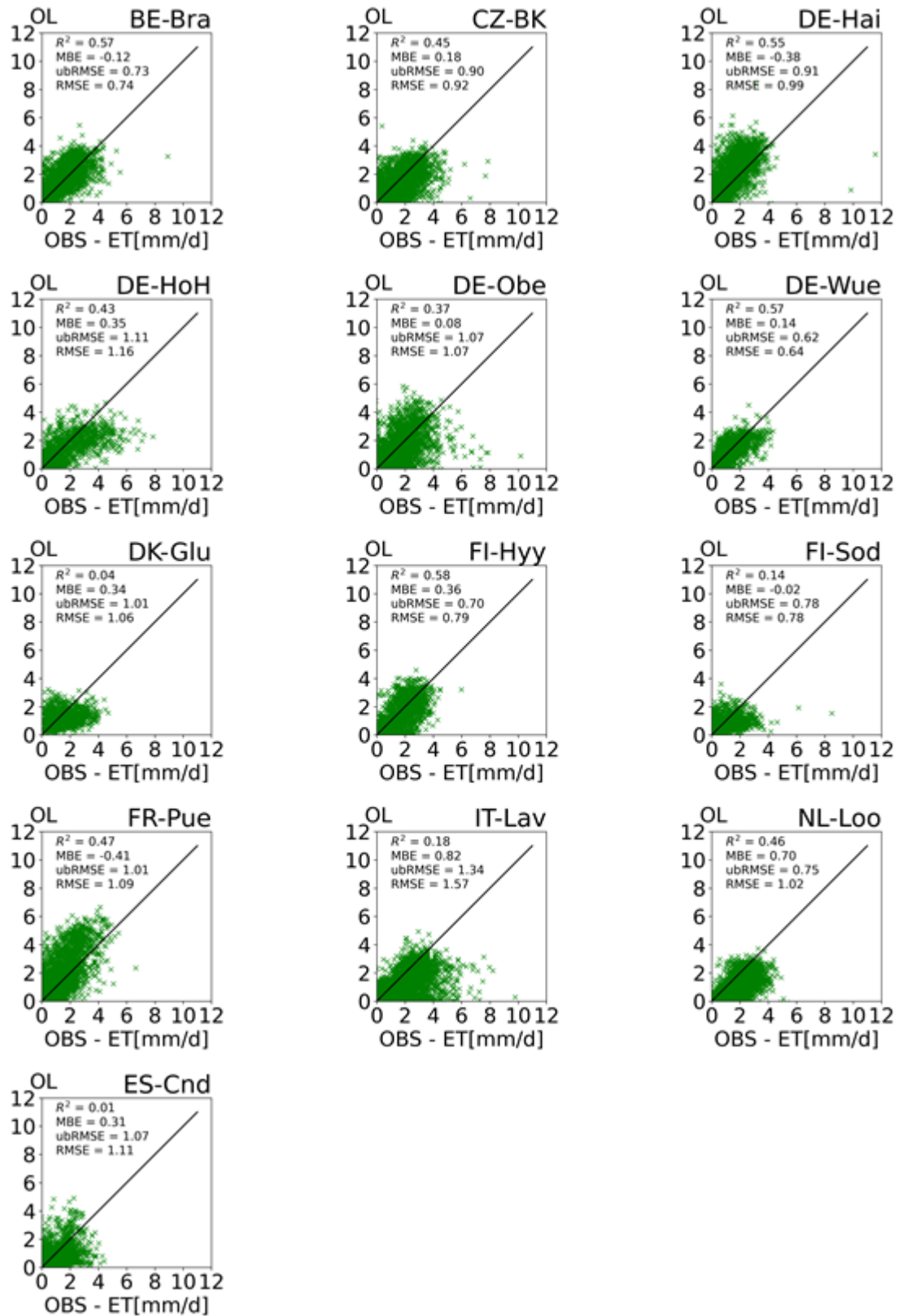
Form
Schrift

Form
12 Pt.

Form
Schrift

Form
12 Pt.

Form
Schrift



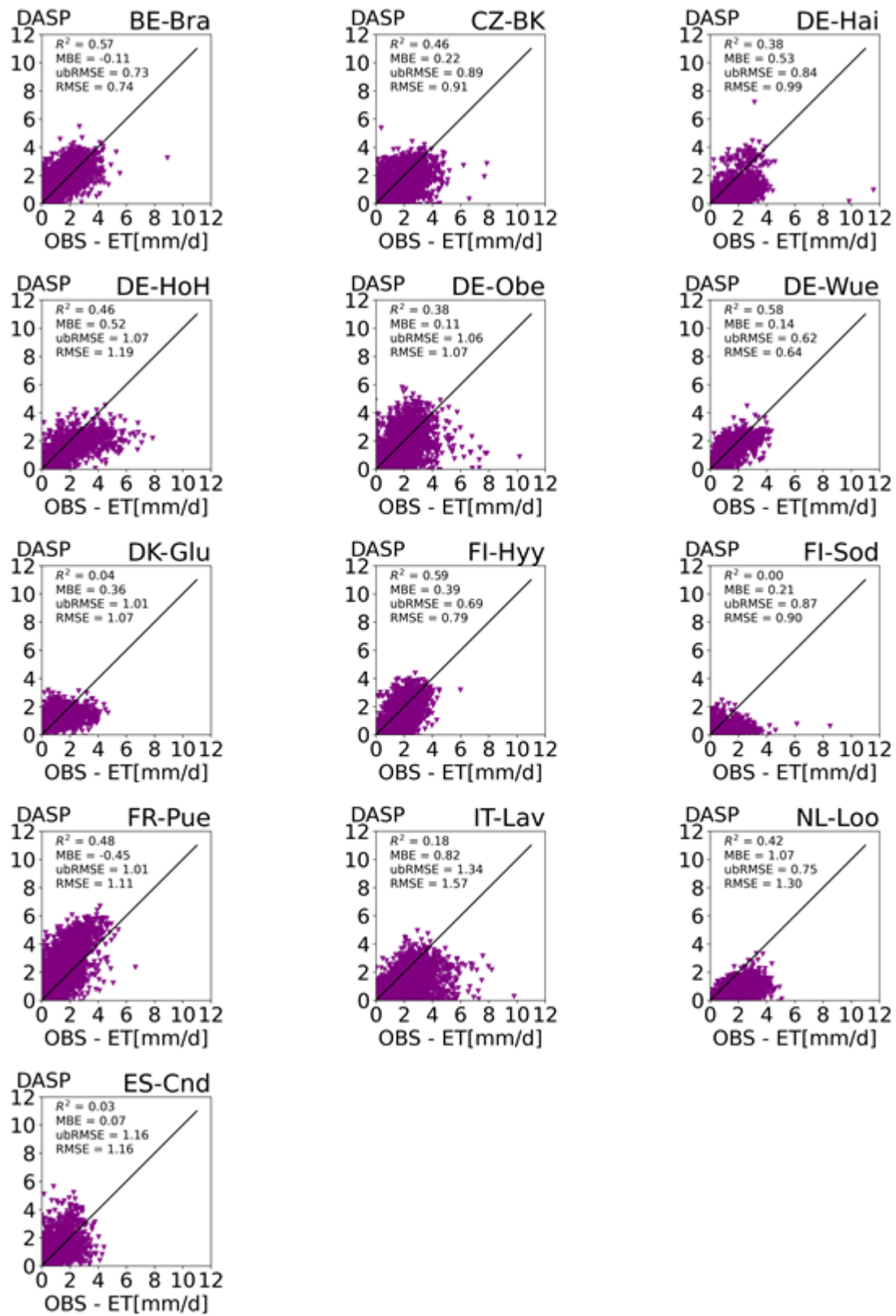
768

769

770

771

Figure 6: Scatter plots of observed evapotranspiration at thirteen study sites versus OL simulation results. The points represent daily averages for the days on which observation data are available.



775

776 **Figure 7:** Scatter plots of observed evapotranspiration at thirteen study sites versus DASP simulation results. The points represent daily averages for the days on which observation data are available.

Form
Schrift
Pt., Z.
Form
12 Pt.

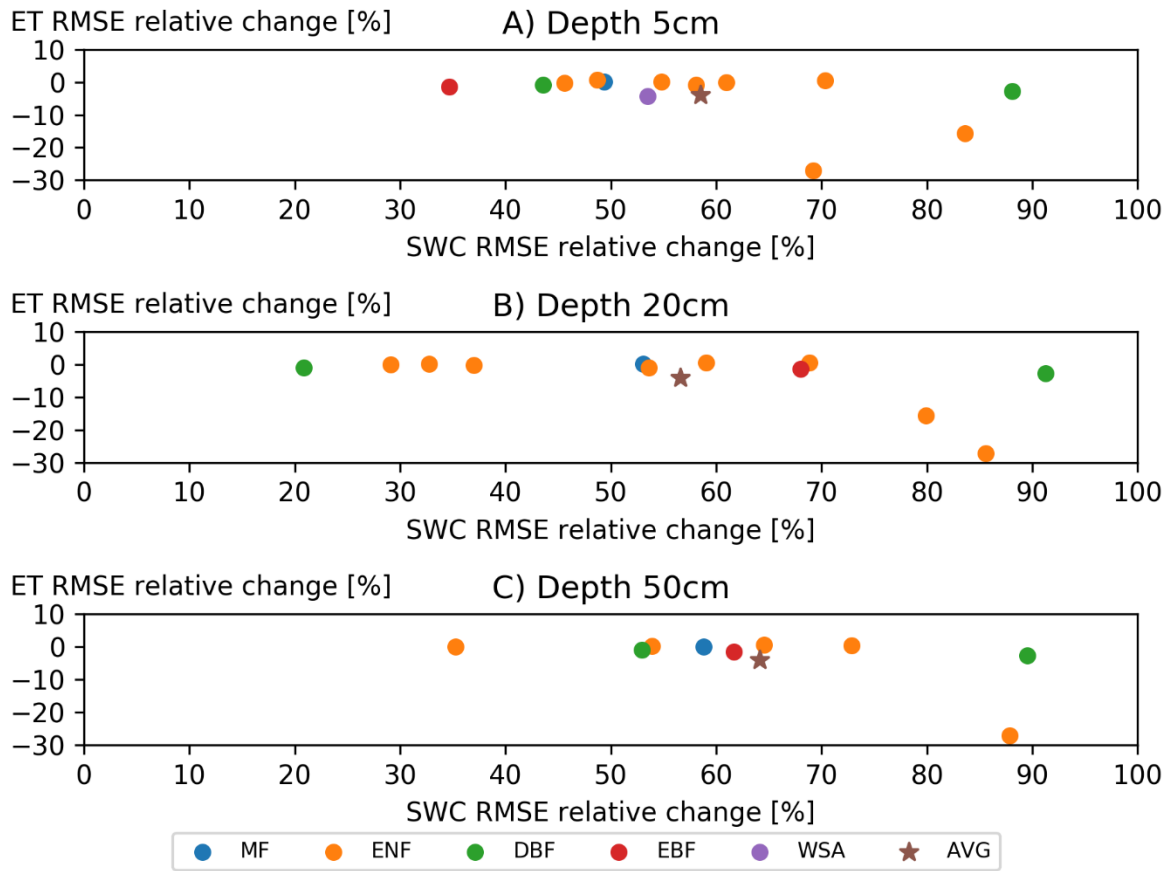


Figure 8: Comparing the SWC and ET characterization for the OL and DASP simulations. Each point represents the overall average RMSE change for one site. The color of the points indicates the classification code for the different forest types (MF: mixed forest, ENF: evergreen needle leaf forest, DBF: deciduous broad leaf forest, EBF: evergreen broad leaf forest, AVG: average over all forest types).

3.3. Evaluation of other land-atmosphere exchange fluxes

Comparing measured and modeled sensible heat fluxes (SH) are compared to measurements (Figures 910 and 1011), similar R² values are obtained for the OL and the DASP approach. The R² values range from 0.23 to 0.51 with an average of 0.36. This is similar to the ET results, where the R² of measured and modeled (OL and DASP) ET range from 0.01 to 0.58 with an average of 0.37. Comparing Fig. 910 and Fig. 1011 shows the impact of data assimilation of SWC on SH to be small. On average DASP improves the MBE by 4.66 W/m² compared to OL. However, for five of the eight sites the improvement of the MBE is smaller than 1 W/m². But, compared to the ET results data assimilation of SWC reduces the MBE of SH for all sites.

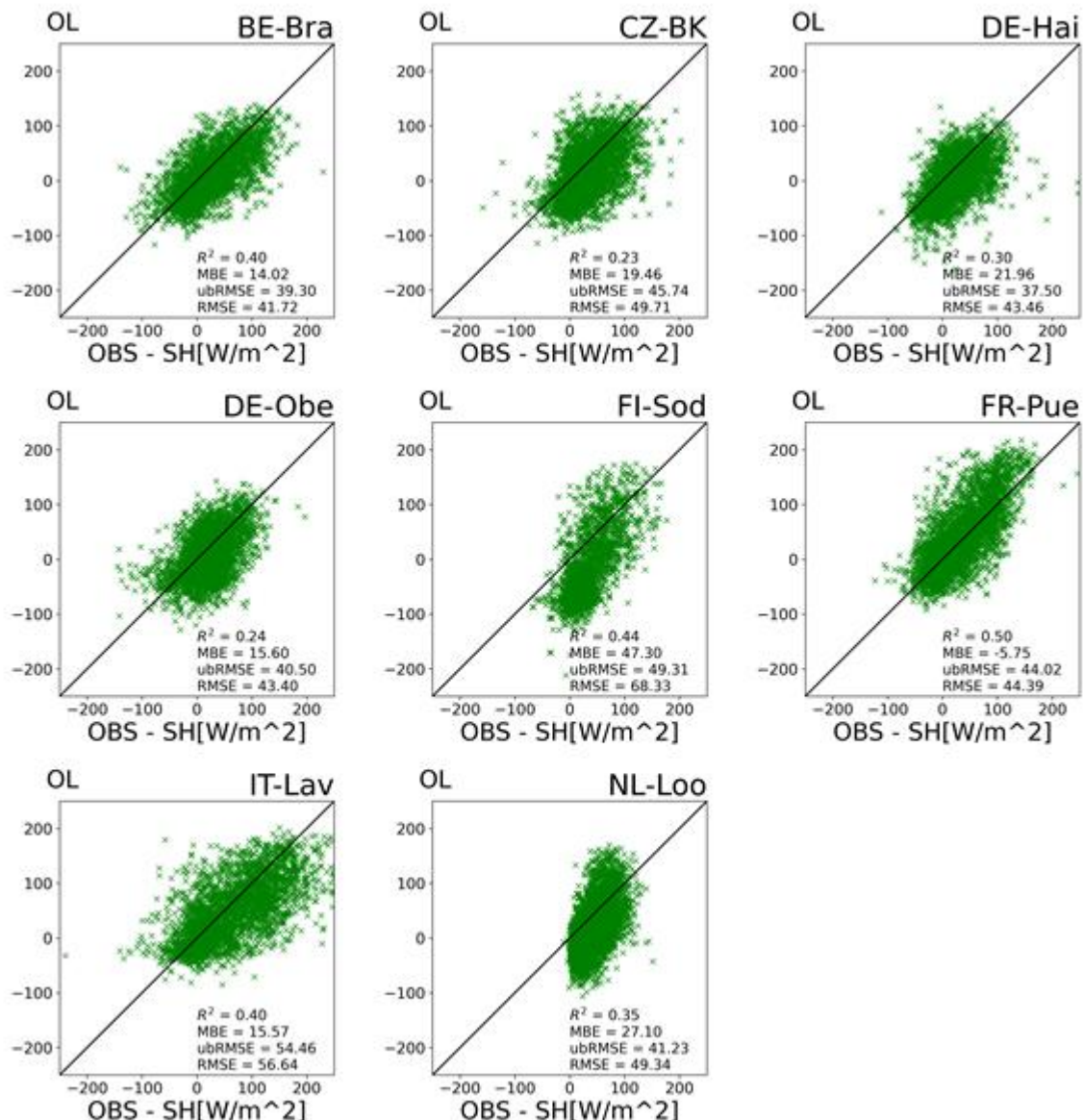
The impact of updating SWC with data assimilation on modeled NEE, GPP, and LAI is shown in Fig. 1112. The NEE is negative (land acts as carbon sink) for eight, seven, and six of the field sites for OL, DAS, and DASP respectively. For DASP the GPP and LAI show an increase for two of the sites, a decrease for three of the sites and remain similar for eight of the sites. Fig. 1213 shows how average SWC in 5 cm and 50 cm depth, ET, NEE, GPP and SH (average over all sites and all years) are

837 affected by data assimilation. Although DASP adjusts SWC at 5cm towards the observations, the
 838 correction for SWC at 50cm depth is smaller because not all sites provide data at this depth. However,
 839 for all sites the data assimilation provides some improvement for SWC estimation even in layers
 840 below the observation depth. In spite of improved SWC characterization, ET deviates slightly more
 841 from the observations after DASP, while sensible heat flux is very slightly closer to the observations.
 842 GPP is lower after DASP and NEE less negative. While the overall change for some of these variables
 843 is small, different variations throughout the year can be observed. This averaging hides the variations
 844 between sites and annual variability but highlights the overall model behavior. Notably, the data
 845 assimilation improves SWC estimation at 5cm throughout the year while at 50 cm depth the
 846 improvement can mainly be observed in late summer and autumn. Similarly, for SH a model structural
 847 bias is apparent with large negative simulated SH values in late autumn, winter, and early spring
 848 while the observations show only a few days with negative average values over all sites and all years.

Form
12 Pt.

Form
12 Pt.

Form
12 Pt.



849

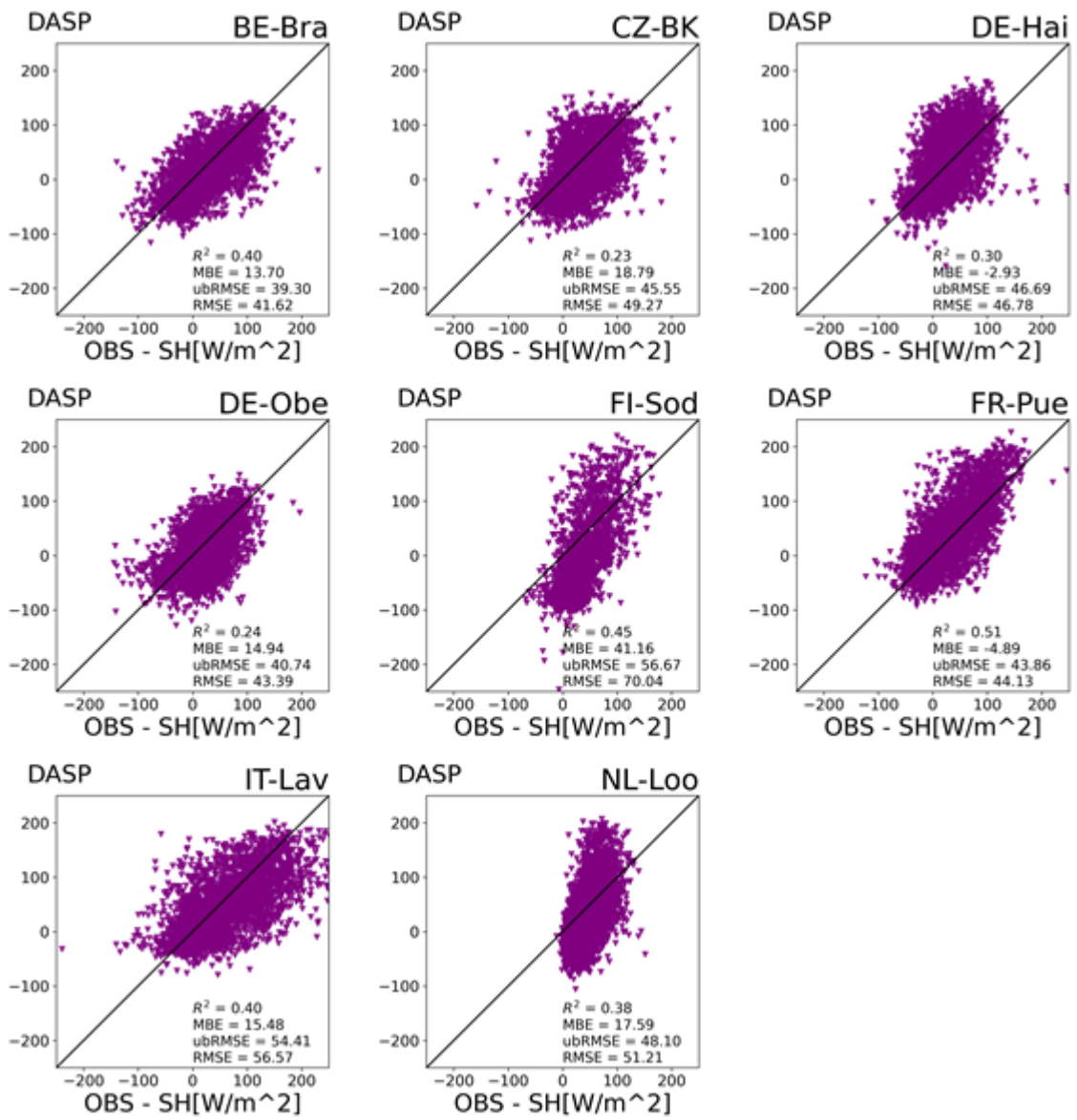
850 Figure 9: Scatter plots of observed sensible heat flux at eight study sites versus OL simulation results.
 851 The points represent daily averages for the days on which observation data are available.

Form
Nicht
Pt., Ze

Form
Pt., Ze

Form
Schrift

Form
12 Pt.



857
858
859
860
861

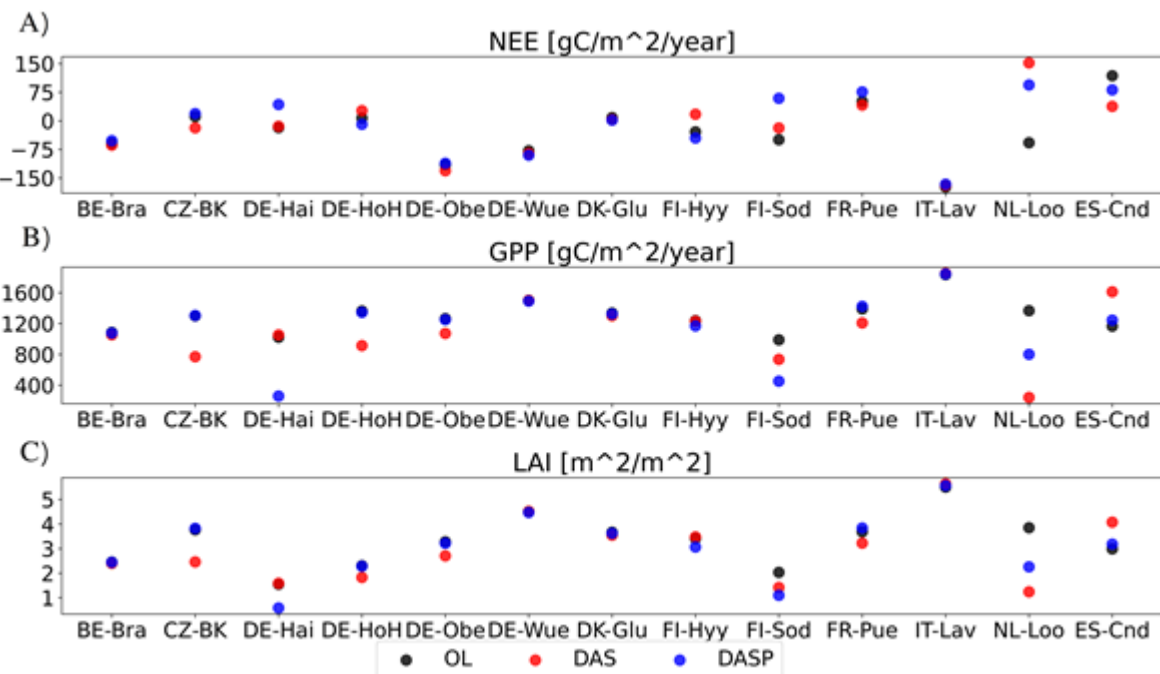
Figure 10: Scatter plots of observed sensible heat flux at eight study sites versus DASP simulation results. The points represent daily averages for the days on which observation data are available.

Form
Fett, S

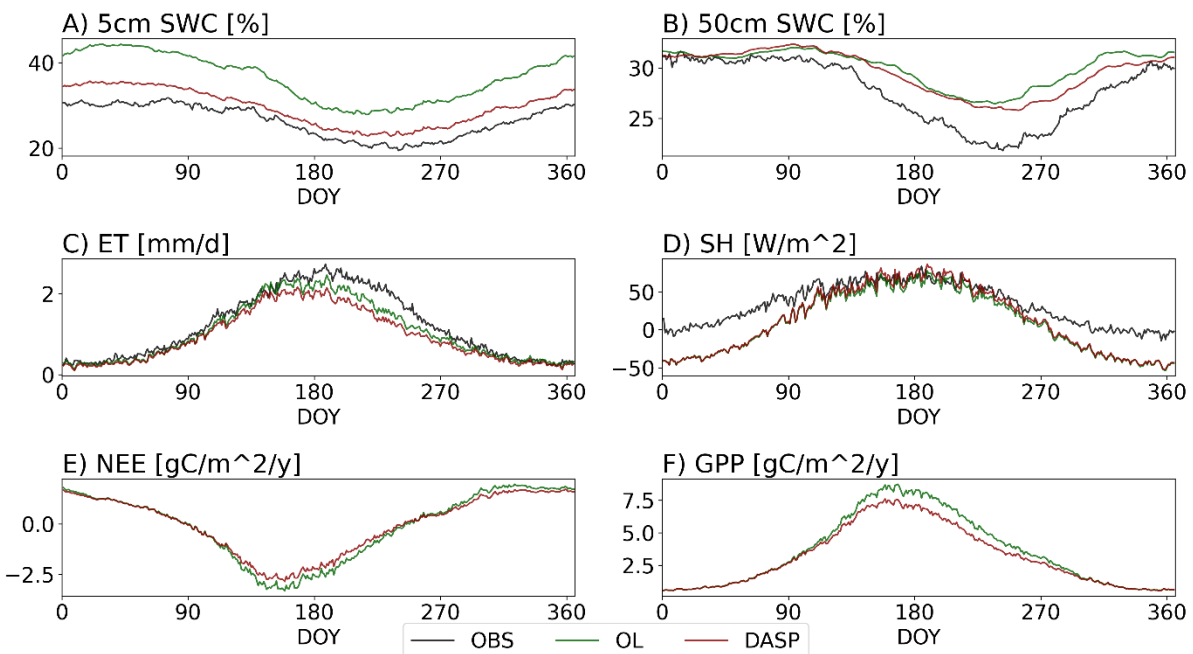
Form
Schrift

Form
12 Pt.

Form
Schrift



871 **Figure 11:** Open loop (OL) and assimilation scenario (DAS and DASP) yearly averages of A) net
 872 ecosystem exchange (NEE), B) gross primary production (GPP), and C) leaf area index (14 shows the
 873 LAI) for each site averaged over all selected sites.



876 **Figure 12:** Seasonality of observed (OBS) and the simulated (OL and DASP) states and fluxes based
 877 on daily averages from all years (2009 to 2018) and all sites: A) soil water content (SWC) at 5 cm

882 ~~depth, B) SWC at 50 cm depth, C) evapotranspiration (ET), D) sensible heat flux (SH), E) net
883 ecosystem exchange (NEE), and F) gross primary production (GPP).~~

884

885 . Sites with the same PFT show clear differences in the yearly LAI cycle.

Form
Form
12 Pt.

4. Discussion

4.1 Soil water content improvements

Our results confirm that assimilation of high quality in-situ SWC data improves the prediction of SWC by CLM5, as it has been demonstrated in several other studies (Hung et al., 2022; Mahmood et al., 2019; Naz et al., 2019; Liu and Mishra, 2017; Han et al., 2015). In our study, we were able to show that this also applies to forest sites with different climates, tree species, and soil properties.

Additionally, CRNS observations represent SWC for a larger area in better correspondence to the EC tower footprint. So far, only few studies have used CRNS information in a data assimilation framework (Rosolem et al., 2014; Han et al., 2015; Baatz et al., 2017, Patil et al., 2021). In line with our study, these studies show the high potential of CRNS for improved soil moisture prediction with land surface models, both in terms of SWC prediction as well as in improving soil hydraulic parameters. Currently, CRNS stations are operated with increasing numbers worldwide (Andreasen et al., 2017), in hydrological observatories (e.g. Bogena et al., 2018; Lui et al., 2018), as national networks (Zreda et al., 2012; Evans et al., 2016) or even increasing at continental scales (e.g. Hawdon et al., 2014; Bogena et al., 2022), which opens up new opportunities for assimilation of CRNS data in land surface models at various scales.

In our data assimilation approach, we assumed that the CRNS signal shows a constant sensitivity to SWC down to the penetration depth of the CRNS. However, Schrön et al. (2017) have shown that the integrated neutron signal over a vertical soil column exhibits a strong decrease in sensitivity with depth and suggested that this physical behavior of neutrons should be taken into account in model applications. For example, Shuttleworth et al. (2013) developed a simple, physically-based analytical model to translate model-predicted soil moisture profiles into aboveground fast neutron counts within a data assimilation framework. A simpler method was proposed by Schrön et al. (2017) by using vertical weighting functions that depend on SWC, atmospheric pressure, horizontal distance and vegetation height. Therefore, in a follow-up study, we will test whether observation operators that account for the vertical weights of the different model soil layers according to the decreasing sensitivity of CRNS with depth will improve our SWC prediction results.

4.2 Evapotranspiration estimation without improvements from SWC DA

Several studies have demonstrated the potential of improved ET prediction using data assimilation of SWC measurements (Liu and Mishra, 2017; Girotto et al., 2017; Lidard et al., 2011). These studies focused on regional or global scale and show heterogeneous spatial patterns of improvement to ET estimation. Baatz et al. (2017) showed that assimilation of CRNS observations altered the ET estimation in CLM4.5 in parts of their study area by up to 80 mm per year compared to the OL approach.

However, in our study with the land surface model CLM5 that data assimilation of SWC does not improve the ET prediction for European forest sites. We also found that the impact on ET from assimilating CRNS observations is similarly limited as assimilation of other in-situ SWC data. Since our study sites cover a variety of climates and soil types, we assume that this result also applies to other forest sites worldwide with similar tree species.

The lack of improvement in ET prediction in the case of data assimilation of in-situ soil moisture information is consistent with findings from other studies. Girotto et al. (2017) found a decrease in ET accuracy after assimilating GRACE data over India and attributed the results to the representation of irrigation in the model. Similarly, Peters-Lidard et al. (2011) showed mixed results after

assimilating multiple satellite soil water content products over North America with spatial variation of improvements and deterioration of ET estimation. Overall, for 9 of the 13 forested study sites our OL simulations show positive mean bias error indicating that CLM5 underestimates the ET compared to the FLUXNET observations. These underestimations ~~are in agreement~~ agree with the results shown in the study by Cheng et al. (2021) showing that CLM5 underestimates ET observations. Additionally, Nearing et al. (2018) investigated the contribution of model structural errors and model inputs for four different LSM and concluded that SWC uncertainty was dominated by soil parameter uncertainty while ET uncertainty was dominated by forcing uncertainty. Without a similar in-depth benchmark study for CLM5, but from our results and the results of the previously mentioned CLM5 studies a similar conclusion can be drawn for CLM5.

A different aspect is that we assume that the EC data are correct to validate our simulation results. However, the EC-data might be affected by energy balance closure issues (Foken, 2008; Hendricks Franssen et al., 2010).

4.4 Methods to improve ET estimation

There are various approaches to improve modeled ET estimates. For example, Zhang et al. (2020) identified and optimized four hydraulic and three vegetation parameters in CLM4.0 that improved ET estimation by 7.3% for the optimization period and 5.3% for the validation period for China. Similarly, Post et al., (2017) calibrated eight parameters to improve NEE estimation in CLM 4.5 and a similar approach to optimize vegetation parameters in CLM 5.0 for ET estimation could improve simulation results. Tang et al. (2015) implemented a root hydraulic redistribution model in CLM4.5 to improve ET estimation but found that their method was only able to improve ET predictions north of 20°N. They identified the representation of deep roots, soil hydraulic parameterization for certain soils, meteorological forcings, and the parameterization of the water table dynamics and drainage as the main limitations to improve ET by their method.

Denager et al. (2022) used SWC measurements for an agricultural site in Denmark for parameter calibration of soil texture, LAI, stomata conductance and the root distribution in CLM5 and obtained improved energy partitioning of ET and SH. However, they also found it difficult to calibrate the parameters to get an improvement in SH estimation throughout the year and suggested that the difference in energy balance closure between LSMs and EC flux observations contributes to the bias.

Fox et al. (2022) concluded that errors in LAI estimations in LSMs lead to substantial flaws in the representation of carbon, water, and energy fluxes. Furthermore, they conclude that data assimilation to remove bias in LAI improves LSMs results significantly and is advisable until the prognostically modeled LAI improves substantially. For example, Zhang et al. (2016) assimilated remotely sensed LAI data into the Biome-BGC model at two sites and improved both ET and NEE estimates, evaluated with EC tower measurements. Rahman et al. (2022) showed that the joint LAI and topsoil SWC assimilation from satellite products improved the ET estimation for the Contiguous United States compared with independent validation datasets. While data assimilation of topsoil SWC alone only improved the SWC estimation.

As mentioned, LAI is identified as a key variable to improve ET estimation and representation of land carbon processes. Therefore, in future work we will investigate the effects of data assimilation of LAI and joint state-vegetation parameter estimation on the simulation of carbon, water, and energy fluxes with CLM5.

Form
Schrift

Form
12 Pt.

Form
Schrift

Form
12 Pt.

Form
Schrift

Form
12 Pt.

Form
Schrift

Form

Form
12 Pt.

Form

Form
Schrift

Form
12 Pt.

Form

Form
12 Pt.

Form

1081 **5. Conclusions**

1082 This paper analyzed the impact of the assimilation of in situ soil water content (SWC) data on SWC
1083 characterization, evapotranspiration (ET), sensible heat flux (SH), gross primary production (GPP)
1084 and net ecosystem exchange (NEE), for 13 forested sites in Europe. Assimilation of SWC, from both
1085 point scale and plot scale observations, with the Ensemble Kalman Filter, using the Community Land
1086 Model version 5 coupled to the Parallel Data Assimilation Framework (CLM5-PDAF) improves
1087 SWC prediction (RMSE reductions between 56% and 64% compared to the open loop run, and
1088 depending on measurement depth). However, assimilation of in situ SWC does not improve the ET
1089 prediction for the investigated European forest sites. For most of the sites, data assimilation showed
1090 almost no effect on ET fluxes (RMSE changes between +/- 1%) and some sites showed strong
1091 negative effects of SWC assimilation on ET predictions (-20% to -30% change in RMSE). The
1092 assimilation of in situ SWC from Cosmic Ray Neutron Sensors (CRNS), which determine SWC over
1093 a larger horizontal footprint more in correspondence with the eddy covariance footprint, for three of
1094 the 13 sites, also does not improve ET characterization. These results suggest that improving the
1095 SWC estimation of state-of-the-art LSM such as CLM5 still suffer from uncertainties in is not
1096 sufficient to improve ET estimation for forest sites. To improve ET estimation it is also necessary to
1097 consider the representation of soil hydrological processes in forests, e.g. deep root LAI in magnitude
1098 and timing, as well as uncertainties in water uptake, uncertainties in the representation of biological
1099 processes of tree transpiration, partly related to uncertain by roots and vegetation parameters. In the
1100 future, to improve modeled ET using data assimilation we will further examine the potential of
1101 assimilating different state variables, like for example leaf area index and updating related vegetation
1102 parameters. In addition, we will apply a measurement operator in the data assimilation framework
1103 that considers the vertical sensitivity of the CRNS signal.

Form
12 Pt.

Form

Form
Schrift

Form

Form
Schrift

Form

Form
Schrift

Form

Form

Form

Form
Schrift

1112 **Figures**

1113 ~~///In the text for now///~~

1114 **Tables**

1115 ~~**Table 1:** Overview of the study sites. Classification uses the International Geosphere Biosphere~~
1116 ~~Program Code (IGBP) as is used for FLUXNET: MF for mixed forests, ENF for evergreen needle~~
1117 ~~leaf forests, DBF for deciduous broad leaf forests, EBF for evergreen broad leaf forests, WSA for~~
1118 ~~woody savannah. LON is longitude and LAT latitude.~~

Form
Form
Form
12 Pt.
Form
Form

Site name	Country	Abbreviation	Code	LON	LAT	Data source	Mean	annual	Mean annual precipitation	Typical tree species
							temperature [°C]	[mm]		
Brassehaat	Belgium	BE-Bra	MF	4.51	51.30	FLUXNET	9.8	750		Scots pine
Bílý Kříž forest	Czech Republic	CZ-BK	ENF	18.53	49.50	FLUXNET	7	1316		Norway spruce
Hainich	Germany	DE-Hai	DBF	10.45	51.07	FLUXNET	8.3	720		Mixed Beech
Hohes Holz	Germany	DE-HoH	DBF	11.21	52.08	COSMOS Europe	10	820		Mixed beech
Oberbärenburg	Germany	DE-Obe	ENF	13.72	50.78	FLUXNET	5.5	996		Norway spruce
Wüstebach	Germany	DE-Wue	ENF	6.33	50.50	COSMOS Europe	7	1180		Spruce
Gladsted	Denmark	DK-Glu	ENF	9.33	56.07	COSMOS Europe	8.2	1080		Spruce
Conde	Spain	ES-Cnd	WSA	3.22	37.91	FLUXNET	15.8	474		Olive grove
Hyytiälä	Finland	FI-Hyy	ENF	24.29	61.84	LTER Europe	3.8	709		Boreal Scots pine
Sodankylä	Finland	FI-Sod	ENF	26.63	67.36	FLUXNET	4	500		Boreal Scots pine
Puéchabon	France	FR-Pue	EBF	3.59	43.69	FLUXNET	13.5	883		Evergreen oak
Lavarone	Italy	IT-Lav	ENF	11.28	45.95	FLUXNET	7.8	1291		Coniferous forest
Loobes	Netherlands	NL-Loo	ENF	5.74	52.16	FLUXNET	9.8	786		Scots pine

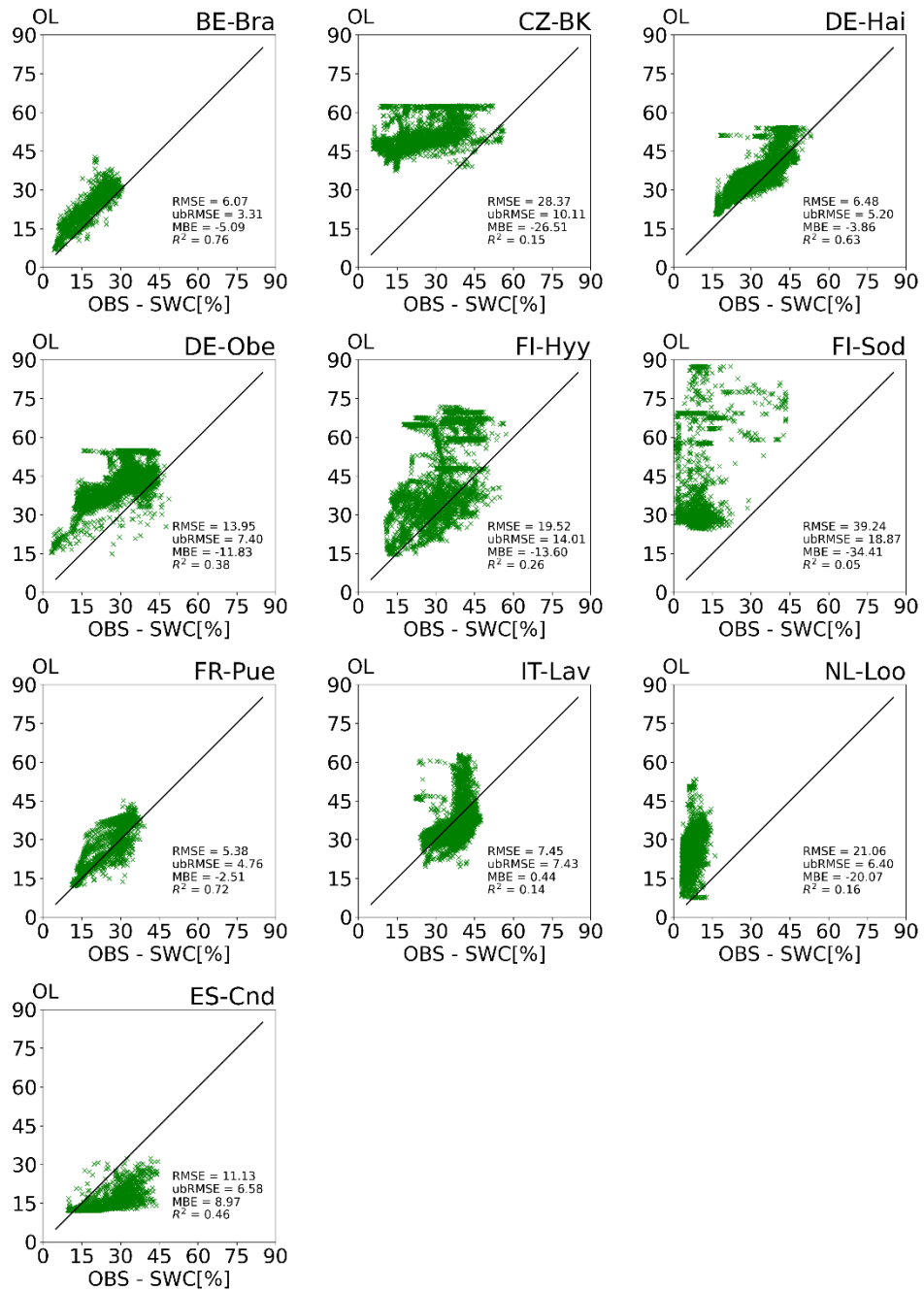


Figure A1: Scatter plots of observed soil water content at ten study sites versus OL simulation results at 5 cm depth. The points represent daily averages for the days on which observation data are available.

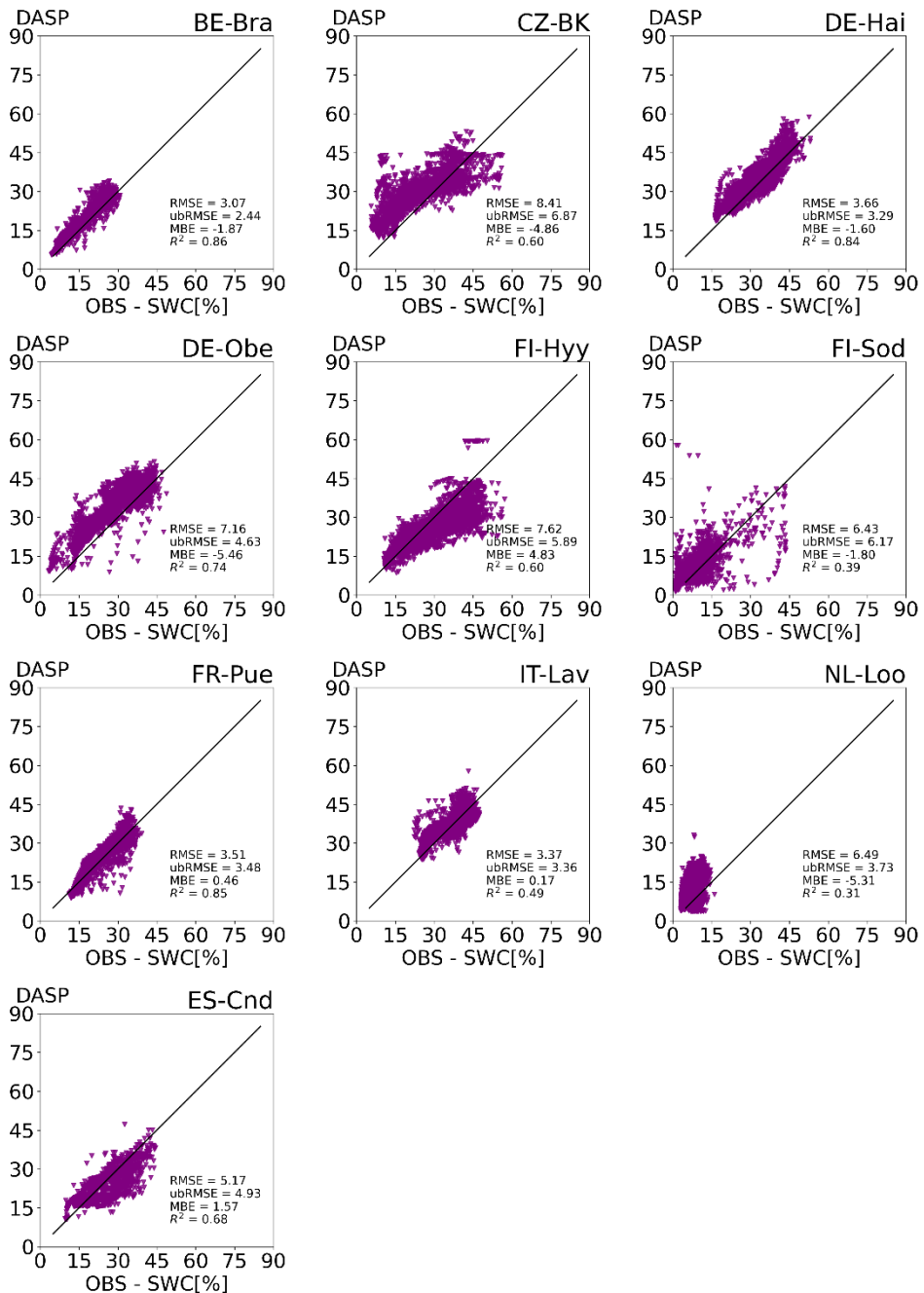


Figure A2: Scatter plots of observed soil water content at ten study sites versus DASP simulation results.

at 5 cm depth. The points represent daily averages for the days on which observation data are available.

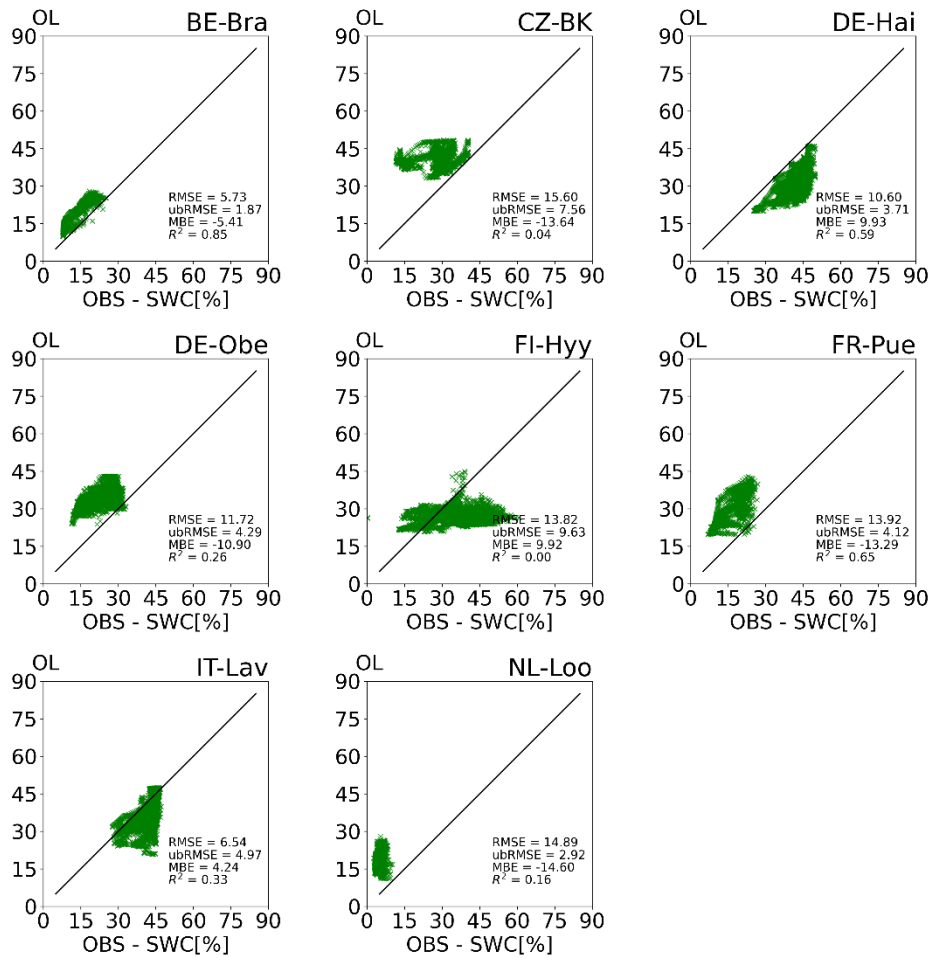
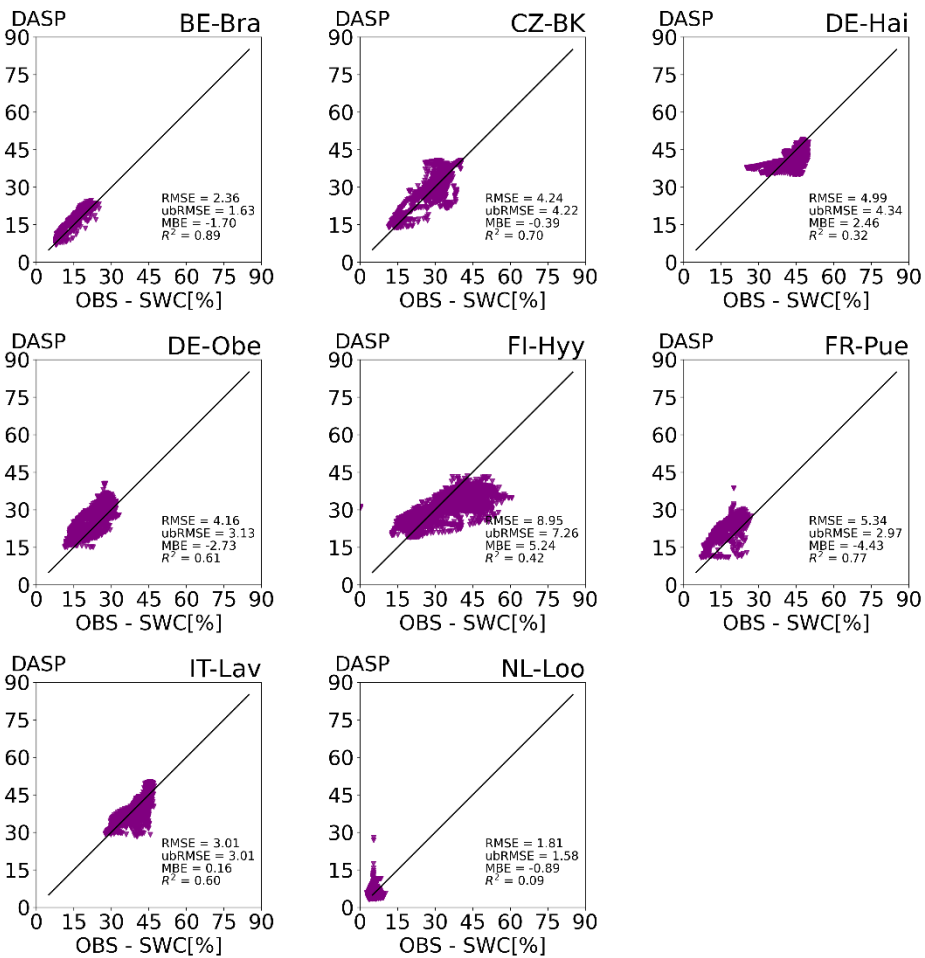


Figure A3: Scatter plots of observed soil water content at eight study sites versus OL simulation results at 50 cm depth. The points represent daily averages for the days on which observation data are available.



1160 **Figure A4:** Scatter plots of observed soil water content at eight study sites versus DASP simulation results at 50 cm depth. The points represent daily averages for the days on which observation data are available.

Code availability.

The code used in this study is available at <https://github.com/HPSCTerrSys/TSMP>.

Data availability.

1165 Data for the European FLUXNET sites is available at <http://www.europe-fluxdata.eu/>. Some additional data used in this study is from the eLTER data portal (<https://data.lter-europe.net/>) and ICOS data portal (<https://www.icos-cp.eu/>). The CRNS data is published in “Dataset of COSMOS Europe: A European network of Cosmic Ray Neutron Soil Moisture Sensors” available at <https://doi.org/10.34731/x9s3-kr48> (Bogena and Neff, 2021).

1170 **Competing interests.** The authors declare that they have no conflict of interest.

Author contribution:

L.S. pre-processed the data, adjusted the code, performed the simulations, and prepared the manuscript. M.A. and S.A. provided data and contributed to the manuscript. H.B., H.J.H.F., and H.V. supervised the research, co-designed the experiments, and contributed to the manuscript.

Acknowledgements:

The authors gratefully acknowledge the support by the project “LIFE RESILIENT FORESTS – Coupling water, fire and climate resilience with biomass production from forestry to adapt watersheds to climate change”. Additionally, the authors gratefully acknowledge the support by the Deutsche Forschungsgemeinschaft (DFG, German Research Foundation) – SFB 1502/1 2022 – Projekt number: 450058266. Furthermore, the authors gratefully acknowledge the computing time granted through JARA on the supercomputer JURECA at Forschungszentrum Jülich. We are thankful for all the data provided by FLUXNET, LTER, ICOS, COSMOS Europe projects and we thank the site PI and technical staff of the sites shown in this study.

For
Sch
For
Sch
For
12
For
Sch
For
ze
For
Sch
For
Zeit
For
Sch

References

1235 Arora, V. K., Katavouta, A., Williams, R. G., Jones, C. D., Brovkin, V., Friedlingstein, P., Schwinger, J.,
Bopp, L., Boucher, O., Cadule, P., Chamberlain, M. A., Christian, J. R., Delire, C., Fisher, R. A., Hajima,
T., Ilyina, T., Joetzjer, E., Kawamiya, M., Koven, C. D., Krasting, J. P., Law, R. M., Lawrence, D. M.,
Lenton, A., Lindsay, K., Pongratz, J., Raddatz, T., Séférian, R., Tachiiri, K., Tjiputra, J. F., Wiltshire, A.,
Wu, T., and Ziehn, T.: Carbon–concentration and carbon–climate feedbacks in CMIP6 models and their
1240 comparison to CMIP5 models, *Biogeosciences*, 17, 4173–4222, <https://doi.org/10.5194/bg-17-4173-2020>, 2020.

1245 Baatz, R., Hendricks Franssen, H.-J., Han, X., Hoar, T., Bogena, H. R., and Vereecken, H.: Evaluation of
a cosmic-ray neutron sensor network for improved land surface model prediction, *Hydrol. Earth Syst.
Sci.*, 21, 2509–2530, <https://doi.org/10.5194/hess-21-2509-2017>, 2017.

1250 Baldocchi, D. D. (2020). How eddy covariance flux measurements have contributed to our understanding
of Global Change Biology. In Global Change Biology (Vol. 26, Issue 1).
<https://doi.org/10.1111/gcb.14807>

1255 Boas, T., Bogena, H., Grünwald, T., Heinesch, B., Ryu, D., Schmidt, M., Vereecken, H., Western, A.,
and Hendricks Franssen, H.-J.: Improving the representation of cropland sites in the Community Land
Model (CLM) version 5.0, *Geosci. Model Dev.*, 14, 573–601, <https://doi.org/10.5194/gmd-14-573-2021>,
2021.

1260 Bogena, H. R., Schrön, M., Jakobi, J., Ney, P., Zacharias, S., Andreasen, M., Baatz, R., Boorman, D.,
Duygu, M. B., Eguíbar-Galán, M. A., Fersch, B., Franke, T., Geris, J., González Sanchis, M., Kerr, Y.,
Korf, T., Mengistu, Z., Mialon, A., Nasta, P., Nitychoruk, J., Pisinaras, V., Rasche, D., Rosolem, R., Said,
H., Schattan, P., Zreda, M., Achleitner, S., Albentosa-Hernández, E., Akyürek, Z., Blume, T., del Campo,
A., Canone, D., Dimitrova-Petrova, K., Evans, J. G., Ferraris, S., Frances, F., Gisolo, D., Güntner, A.,
Herrmann, F., Iwema, J., Jensen, K. H., Kunstmänn, H., Lidón, A., Looms, M. C., Oswald, S.,
Panagopoulos, A., Patil, A., Power, D., Rebmann, C., Romano, N., Scheiffele, L., Seneviratne, S., Weltin,
G., and Vereecken, H.: COSMOS-Europe: a European network of cosmic-ray neutron soil moisture
sensors, *Earth Syst. Sci. Data*, 14, 1125–1151, <https://doi.org/10.5194/essd-14-1125-2022>, 2022.

Bogena, Heye; Ney, Patrizia (2021): Dataset of "COSMOS-Europe: A European network of Cosmic-Ray Neutron Soil Moisture Sensors"(Dataset). Forschungszentrum Jülich, <https://doi.org/10.34731/x9s3-kr48>.

1305 Bollmeyer, C., Keller, J.D., Ohlwein, C., Wahl, S., Crewell, S., Friederichs, P., Hense, A., Keune, J., Kneifel, S., Pscheidt, I., Redl, S. and Steinke, S. (2015), Towards a high-resolution regional reanalysis for the European CORDEX domain. *Q.J.R. Meteorol. Soc.*, 141: 1-15. <https://doi.org/10.1002/qj.2486> <https://doi.org/10.1002/qj.2486>

1310 Burgers, G., Jan van Leeuwen, P., and Evensen, G.: Analysis scheme in the ensemble Kalman filter, *Mon. Weather Rev.*, 126, 1719–1724, 1998.

1315 Cheng, Y., Huang, M., Zhu, B., Bisht, G., Zhou, T., Liu, Y., et al. (2021). Validation of the Community Land Model version 5 over the contiguous United States (CONUS) using in situ and remote sensing data sets. *Journal of Geophysical Research: Atmospheres*, 126, e2020JD033539. <https://doi.org/10.1029/2020JD033539> <https://doi.org/10.1029/2020JD033539>

1320 Clapp, R. B. and Hornberger, G. M.: Empirical equations for some soil hydraulic properties, *Water Resour. Res.*, 14, 601–604, 1978.

1325 Denager, T., Sonnenborg, T. O., Looms, M. C., Bogena, H., and Jensen, K. H.: Multi-objective calibration of the Community Land Model Version 5.0 using in-situ observations of water and energy fluxes and variables, EGUsphere [preprint], <https://doi.org/10.5194/egusphere-2022-406>, 2022.

1330 Dirmeyer, P.A., Chen, L., Wu, J., Shin, C.-S., Huang, B., Cash, B.A., Bosilovich, M.G., Mahanama, S., Koster, R.D., Santanello, J.A., Ek, M.B., Balsamo, G., Dutra, E. and Lawrence, D.M. (2018) Verification of land–atmosphere coupling in forecast models, reanalyses, and land surface models using flux site observations. *Journal of Hydrometeorology*, 19(2), 375–392.

1335 Dombrowski, O., Brogi, C., Hendricks Franssen, H.-J., Zanotelli, D., and Bogena, H.: CLM5-FruitTree: a new sub-model for deciduous fruit trees in the Community Land Model (CLM5), *Geosci. Model Dev.*, 15, 5167–5193, <https://doi.org/10.5194/gmd-15-5167-2022>, 2022.

Evensen, G.: Sequential data assimilation with a nonlinear quasi-geostrophic model using Monte Carlo methods to forecast error statistics, *J. Geophys. Res.-Oceans*, 99, 10143–10162, 1994.

1375 Fertig, E., Baek, S.-J., Hunt, B., Ott, E., Szunyogh, I., Aravéquia, J., Kalnay, E., Li, H., and Liu, J.:
Observation bias correction with an ensemble Kalman filter, *Tellus A*, 61, 210–226, 2009.

1380 Foken, T. (2008), THE ENERGY BALANCE CLOSURE PROBLEM: AN OVERVIEW. *Ecological Applications*, 18: 1351-1367. <https://doi.org/10.1890/06-0922.1>

1385 Friedland, B.: Treatment of bias in recursive filtering, *IEEE T. Automat. Contr.*, 14, 359–367, 1969.

1390 Girotto, M., Lannoy, G. J., Reichle, R. H., Rodell, M., Draper, C., Bhanja, S. N., & Mukherjee, A. (2017). Benefits and pitfalls of GRACE data assimilation: A case study of terrestrial water storage depletion in India. *Geophysical Research Letters*, 44, 4107–4115. <https://doi.org/10.1002/2017GL072994>

1395 Han, X., Li, X., He, G., Kumbhar, P., Montzka, C., Kollet, S., Miyoshi, T., Rosolem, R., Zhang, Y., Vereecken, H., and Franssen, H.-J. H.: DasPy 1.0 – the Open Source Multivariate Land Data Assimilation Framework in combination with the Community Land Model 4.5, *Geosci. Model Dev. Discuss.*, <https://doi.org/10.5194/gmdd-8-7395-2015>, 2015a.

1400 Han, X., Franssen, H.-J. H., Rosolem, R., Jin, R., Li, X., and Vereecken, H.: Correction of systematic model forcing bias of CLM using assimilation of cosmic-ray Neutrons and land surface temperature: a study in the Heihe Catchment, China, *Hydrol. Earth Syst. Sci.*, 19, 615–629, <https://doi.org/10.5194/hess-19-615-2015>, 2015.

1405 Hudiburg, T. W., Law, B. E., and Thornton, P. E.: Evaluation and improvement of the Community Land Model (CLM4) in Oregon forests, *Biogeosciences*, 10, 453–470, <https://doi.org/10.5194/bg-10-453-2013>, 2013.

1410 Hung, C. P., Schalge, B., Baroni, G., Vereecken, H., and Hendricks Franssen, H.-J. (2022). Assimilation of groundwater level and soil moisture data in an integrated land surface-subsurface model for southwestern Germany. *Water Resour. Res.* 58, e2021WR031549. doi: 10.1029/2021WR031549

Jung, M., Reichstein, M., Margolis, H. A., Cescatti, A., Richardson, A. D., Arain, M. A., et al. (2011). Global patterns of land-atmosphere fluxes of carbon dioxide, latent heat, and sensible heat derived from

eddy covariance, satellite, and meteorological observations. *J. Geophys. Res.* 116, G00J07. doi: 10.1029/2010jg001566

1450 Kennedy, D., Swenson, S., Oleson, K. W., Lawrence, D. M., Fisher, R., Lola da Costa, A. C., and Gentine, P.: Implementing plant hydraulics in the Community Land Model, version 5, *J. Adv. Model. Earth Sy.*, 11, 485–513, <https://doi.org/10.1029/2018MS001500>, 2019.

1455 Lawrence, D. M., Fisher, R. A., Koven, C. D., Oleson, K. W., Swenson, S. C., Bonan, G., Collier, N., Ghimire, B., van Kampenhout, L., Kennedy, D., Kluzek, E., Lawrence, P. J., Li, F., Li, H., Lombardozzi, D., Riley, W. J., Sacks, W. J., Shi, M., Vertenstein, M., Wieder, W. R., Xu, C., Ali, A. A., Badger, A. M., Bisht, G., Brunke, M. A., Burns, S. P., Buzan, J., Clark, M., Craig, A., Dahlin, K., Drewniak, B., Fisher, J. B., Flanner, M., Fox, A. M., Gentine, P., Hoffman, F., Keppel-Aleks, G., Knox, R., Kumar, S., Lenaerts, J., Leung, L. R., Lipscomb, W. H., Lu, Y., Pandey, A., Pelletier, J. D., Perket, J., Randerson, J. T., Ricciuto, D. M., Sanderson, B. M., Slater, A., Subin, Z. M., Tang, J., Thomas, R. Q., Val Martin, M., and Zeng, X.: The Community Land Model version 5: Description of new features, benchmarking, and impact of forcing uncertainty, *J. Adv. Model. Earth Sy.*, 11, 4245–4287, 2019.

1465 Lawrence, D., Fisher, R., Koven, C., Oleson, K., Swenson, S., Vertenstein, M., Andre, B., Bonan, G., Ghimire, B., van Kam- penhout, L., Kennedy, D., Kluzek, E., Knox, R., Lawrence, P., Li, F., Li, H., Lombardozzi, D., Lu, Y., Perket, P., Riley, W., Sacks, W., Shi, M., Wieder, W., Xu, C., Ali, A., Badger, A., Bisht, G., Broxton, P., Brunke, M., Buzan, J., Clark, M., Craig, T., Dahlin, K., Drewniak, B., Emmons, L., Fisher, J., Flanner, M., Gentine, P., Lenaerts, J., Levis, S., Leung, L., Lipscomb, W., Pelletier, J., Ricciuto, D., Sanderson, B., Shuman, J., Slater, A., Subin, Z., Tang, J., Tawfik, A., Thomas, Q., Tilmes, S., Vitt, and F., Zeng, X.: Technical description of version 5.0 of the Community Land Model (CLM), National Center for Atmospheric Research, University Corporation for Atmospheric Research, Boulder, CO, 2018.

1475 Liu, D.; Mishra, A.K. Performance of AMSR_E soil moisture data assimilation in CLM4.5 model for monitoring hydrologic fluxes at global scale. *J. Hydrol.* 2017, 547, 67–79.

Mahmood, T., Xie, Z., Jia, B. et al. A Soil Moisture Data Assimilation System for Pakistan Using PODEn4DVar and CLM4.5. *J Meteorol Res* 33, 1182–1193 (2019). <https://doi.org/10.1007/s13351-019-9020-2>

1480 Naz, B. S., Kurtz, W., Montzka, C., Sharples, W., Goergen, K., Keune, J., Gao, H., Springer, A., Hendricks Franssen, H.-J., and Kollet, S.: Improving soil moisture and runoff simulations at 3 km over Europe using land surface data assimilation, *Hydrol. Earth Syst. Sci.*, 23, 277–301, <https://doi.org/10.5194/hess-23-277-2019>, 2019.

Nearing, Grey S., Benjamin L. Ruddell, Martyn P. Clark, Bart Nijssen, and Christa Peters-Lidard. "Benchmarking and Process Diagnostics of Land Models", *Journal of Hydrometeorology* 19, 11 (2018): 1835-1852, accessed Dec 15, 2022, <https://doi.org/10.1175/JHM-D-17-0209.1>

1525 Nerger, L., Hiller, W., and Schröter, J.: PDAF-the parallel data assimilation framework: experiences with Kalman filtering, in: Use of high performance computing in meteorology, World Scientific, 63–83, https://doi.org/10.1142/9789812701831_0006, 2005.

1530 Parr, T.W., Ferretti, M., Simpson, I.C. et al. Towards A Long-Term Integrated Monitoring Programme In Europe: Network Design in Theory and Practice. *Environ Monit Assess* 78, 253–290 (2002). <https://doi.org/10.1023/A:1019934919140>

1535 Patil A, Fersch B, Hendricks Franssen H-J and Kunstmann H (2021) Assimilation of Cosmogenic Neutron Counts for Improved Soil Moisture Prediction in a Distributed Land Surface Model. *Front. Water* 3:729592. doi: 10.3389/frwa.2021.729592

1540 Peters-Lidard, C.D., Kumar, S.V., Mocko, D.M. and Tian, Y. (2011), Estimating evapotranspiration with land data assimilation systems. *Hydrol. Process.*, 25: 3979-3992. <https://doi.org/10.1002/hyp.8387>

1545 Rahman, Azbina, Viviana Maggioni, Xinxuan Zhang, Paul Houser, Timothy Sauer, and David M. Mocko. 2022. "The Joint Assimilation of Remotely Sensed Leaf Area Index and Surface Soil Moisture into a Land Surface Model" *Remote Sensing* 14, no. 3: 437. <https://doi.org/10.3390/rs14030437>

1550 Reichle, R. H., Koster, R. D., Liu, P., Mahanama, S. P., Njoku, E. G., and Owe, M.: Comparison and assimilation of global soil moisture retrievals from the Advanced Microwave Scanning Radiometer for the Earth Observing System (AMSR-E) and the Scanning Multichannel Microwave Radiometer (SMMR), *J. Geophys. Res.-Atmos.*, 112, D09108, <https://doi.org/10.1029/2006JD008033>, 2007.

1555 Rosolem, R., Hoar, T., Arellano, A., Anderson, J. L., Shuttleworth, W. J., Zeng, X., and Franz, T. E.: Translating aboveground cosmic-ray neutron intensity to high-frequency soil moisture profiles at sub-kilometer scale, *Hydrol. Earth Syst. Sci.*, 18, 4363–4379, <https://doi.org/10.5194/hess-18-4363-2014>, 2014.

1555 Schrön, M., Köhli, M., Scheiffele, L., Iwema, J., Bogena, H. R., Lv, L., Martini, E., Baroni, G., Rosolem, R., Weimar, J., Mai, J., Cuntz, M., Rebmann, C., Oswald, S. E., Dietrich, P., Schmidt, U., and Zacharias,

S.: Improving calibration and validation of cosmic-ray neutron sensors in the light of spatial sensitivity, *Hydrol. Earth Syst. Sci.*, 21, 5009–5030, <https://doi.org/10.5194/hess-21-5009-2017>, 2017.

1595 Strelbel, L., Bogena, H. R., Vereecken, H., and Hendricks Franssen, H.-J.: Coupling the Community Land Model version 5.0 to the parallel data assimilation framework PDAF: description and applications, *Geosci. Model Dev.*, 15, 395–411, <https://doi.org/10.5194/gmd-15-395-2022>, 2022.

1600 Tang, J., Riley, W. J., and Niu, J. (2015), Incorporating root hydraulic redistribution in CLM4.5: Effects on predicted site and global evapotranspiration, soil moisture, and water storage, *J. Adv. Model. Earth Syst.*, 7, 1828– 1848, doi:10.1002/2015MS000484.

1605 Wilson, D.J., Western, A.W., Grayson, R.B., 2004. Identifying and quantifying sources of variability in temporal and spatial soil moisture observations. *Water Resour. Res.*, 40, W02507, doi:10.1029/2003WR002306

1610 Wurster, Patrick, Marco Maneta, Santiago Beguería, Kelly Cobourn, Bruce Maxwell, Nick Silverman, Stephanie Ewing, et al. 2020. "Characterizing the Impact of Climatic and Price Anomalies on Agrosystems in the Northwest United States." *Agricultural and Forest Meteorology* 280 (November 2018). <https://doi.org/10.1016/j.agrformet.2019.107778>.

1615 Zhang, Chong, Zhenhua Di, Qingyun Duan, Zhenghui Xie, and Wei Gong. 2020. "Improved Land Evapotranspiration Simulation of the Community Land Model Using a Surrogate-Based Automatic Parameter Optimization Method" *Water* 12, no. 4: 943. <https://doi.org/10.3390/w12040943>

1620 Zhang, L., Lei, H., Shen, H., Cong, Z., Yang, D., and Liu, T.: Evaluating the representation of vegetation phenology in the Community Land Model 4.5 in a temperate grassland, *J. Geophys. Res.-Biogeo.*, 124, 187–210, 2019.

1625 Zhang, T., Sun, R., Peng, C. et al. Integrating a model with remote sensing observations by a data assimilation approach to improve the model simulation accuracy of carbon flux and evapotranspiration at two flux sites. *Sci. China Earth Sci.* 59, 337–348 (2016). <https://doi.org/10.1007/s11430-015-5160-0>

Tables

1635 **Table 1:** Overview of the study sites. Classification uses the International Geosphere-Biosphere Program Code (IGBP) as is used for FLUXNET: MF for mixed forests, ENF for evergreen needle leaf forests, DBF for deciduous broad leaf forests, EBF for evergreen broad leaf forests, WSA for woody savannah. LON is longitude and LAT latitude.

<u>Site name</u>	<u>Country</u>	<u>Abbreviation</u>	<u>Code</u>	<u>LON</u>	<u>LAT</u>	<u>Elevation</u> [m.a.s.l.]	<u>Data source</u>	<u>Mean annual temperature</u> [°C]	<u>Mean annual precipitation</u> [mm]	<u>Typical tree species</u>
Brasschaat	Belgium	BE-Bra	MF	4.51	51.3	16	FLUXNET	9.8	750	Scots pine
Bílý Kříž forest	Czech Republic	CZ-BK	ENF	18.53	49.5	875	FLUXNET	7	1316	Norway spruce
Hainich	Germany	DE-Hai	DBF	10.45	51.07	430	FLUXNET	8.3	720	Mixed Beech
Hohes Holz	Germany	DE-HoH	DBF	11.21	52.08	217	COSMOS Europe	10	820	Mixed beech
Oberbärenburg	Germany	DE-Obe	ENF	13.72	50.78	734	FLUXNET	5.5	996	Norway spruce
Wüstebach	Germany	DE-Wue	ENF	6.33	50.5	605	COSMOS Europe	7	1180	Spruce
Gludsted	Denmark	DK-Glu	ENF	9.33	56.07	86	COSMOS Europe	8.2	1080	Spruce
Conde	Spain	ES-Cnd	WSA	-3.22	37.91	370	FLUXNET	15.8	474	Olive grove
Hyytiälä	Finland	FI-Hyy	ENF	24.29	61.84	181	LTER Europe	3.8	709	Boreal Scots pine
Sodankylä	Finland	FI-Sod	ENF	26.63	67.36	180	FLUXNET	-1	500	Boreal Scots pine
Puéchabon	France	FR-Pue	EBF	3.59	43.69	270	FLUXNET	13.5	883	Evergreen oak
Lavarone	Italy	IT-Lav	ENF	11.28	45.95	1353	FLUXNET	7.8	1291	Coniferous forest
Loobos	Netherlands	NL-Loods	ENF	5.74	52.16	25	FLUXNET	9.8	786	Scots pine

1640

Figures

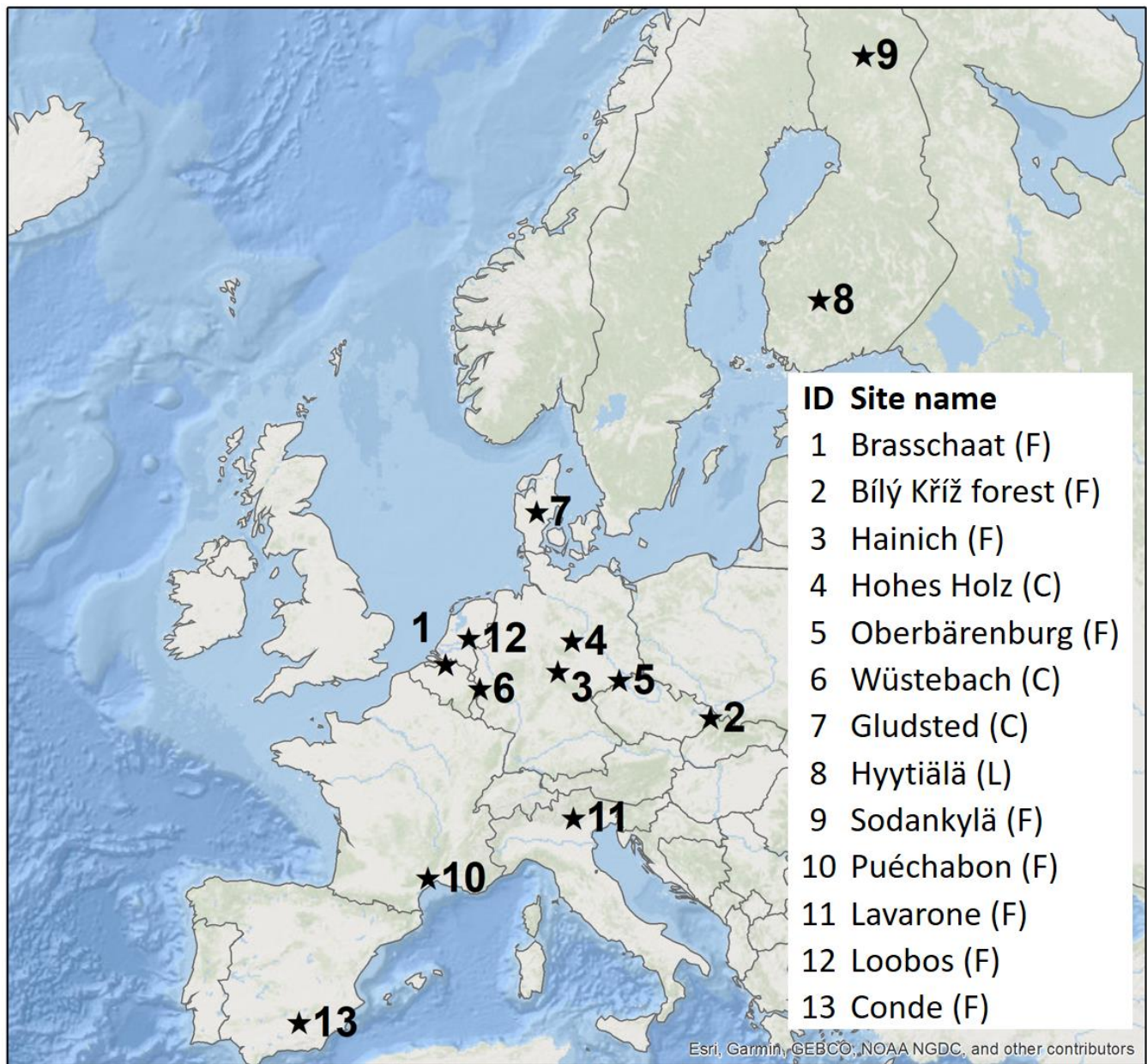


Figure 1: Map showing the location of the selected study sites of the FLUXNET (F), eLTER (L) and COSMOS-Europe (C) networks.

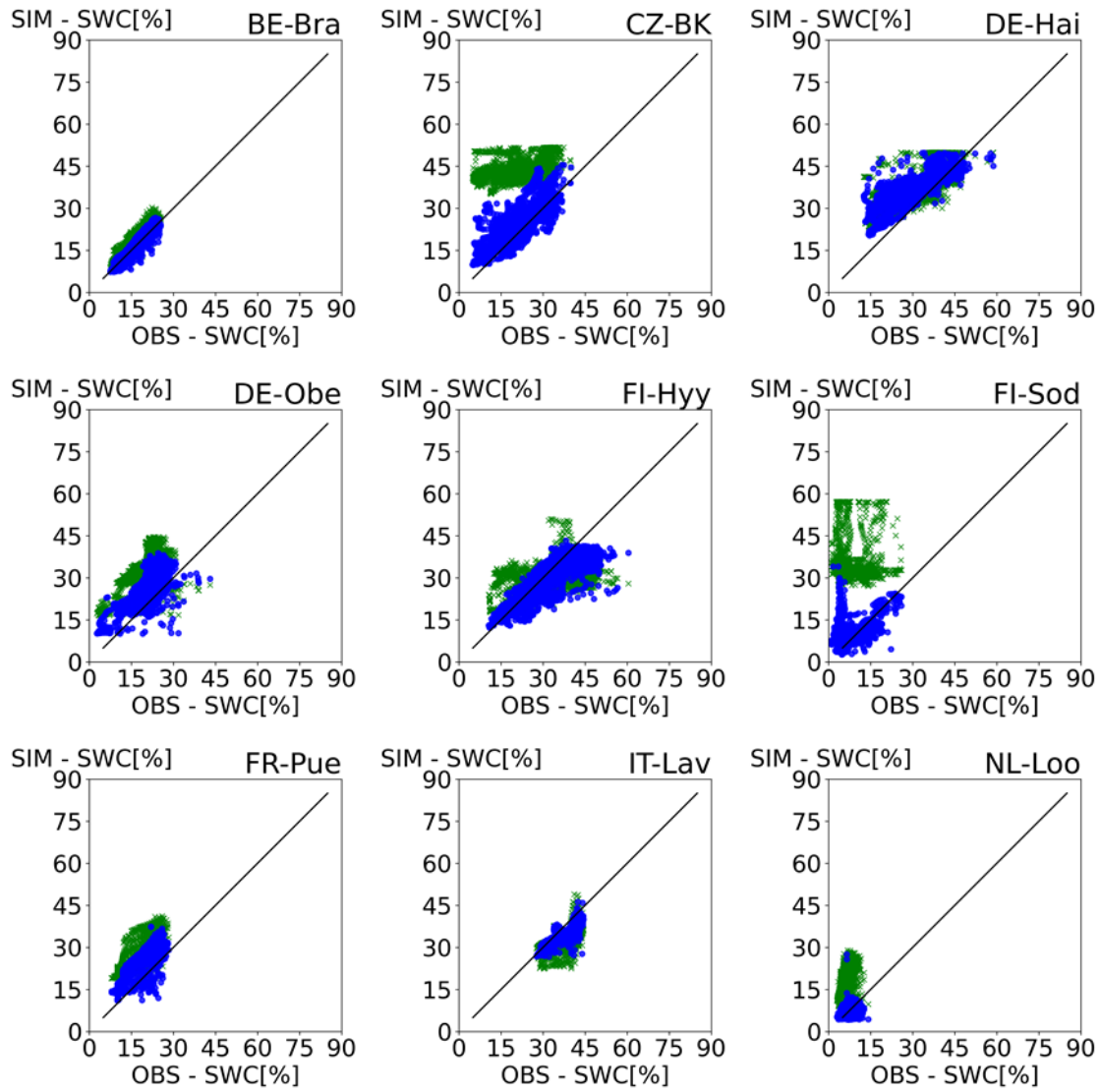


Figure 2: Scatter plots of observed soil water content at 20 cm depth at nine study sites versus OL and DAS simulated soil water content. The points represent daily averages for the days observation data are available. Green points are OL and blue points are DAS results.

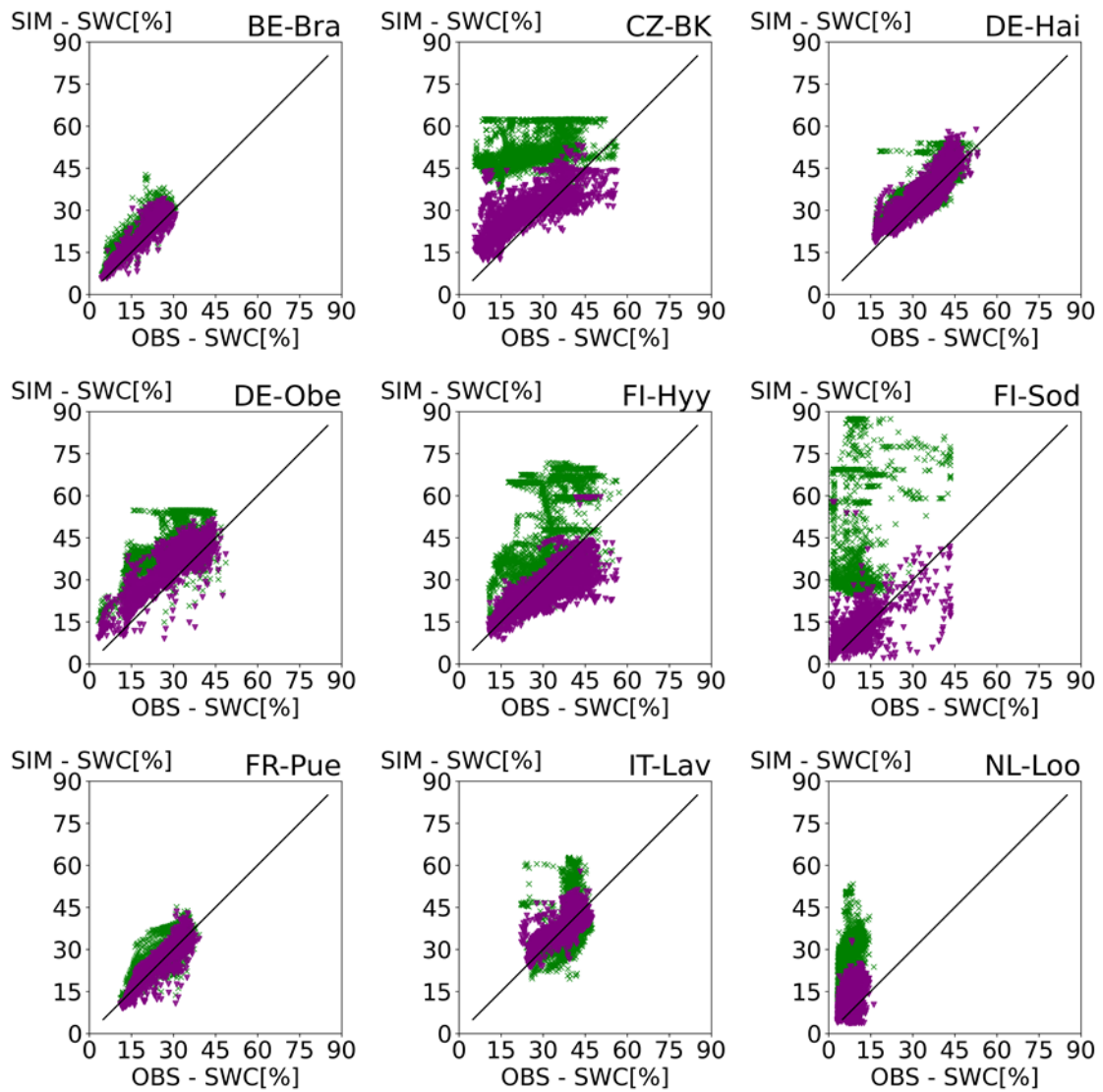


Figure 3: Scatter plots of observed soil water content at 20 cm depth at nine study sites versus OL and DASP simulated soil water content results at 20 cm depth. The points represent daily averages for the days observation data are available. Green points are OL and purple points are DASP results.

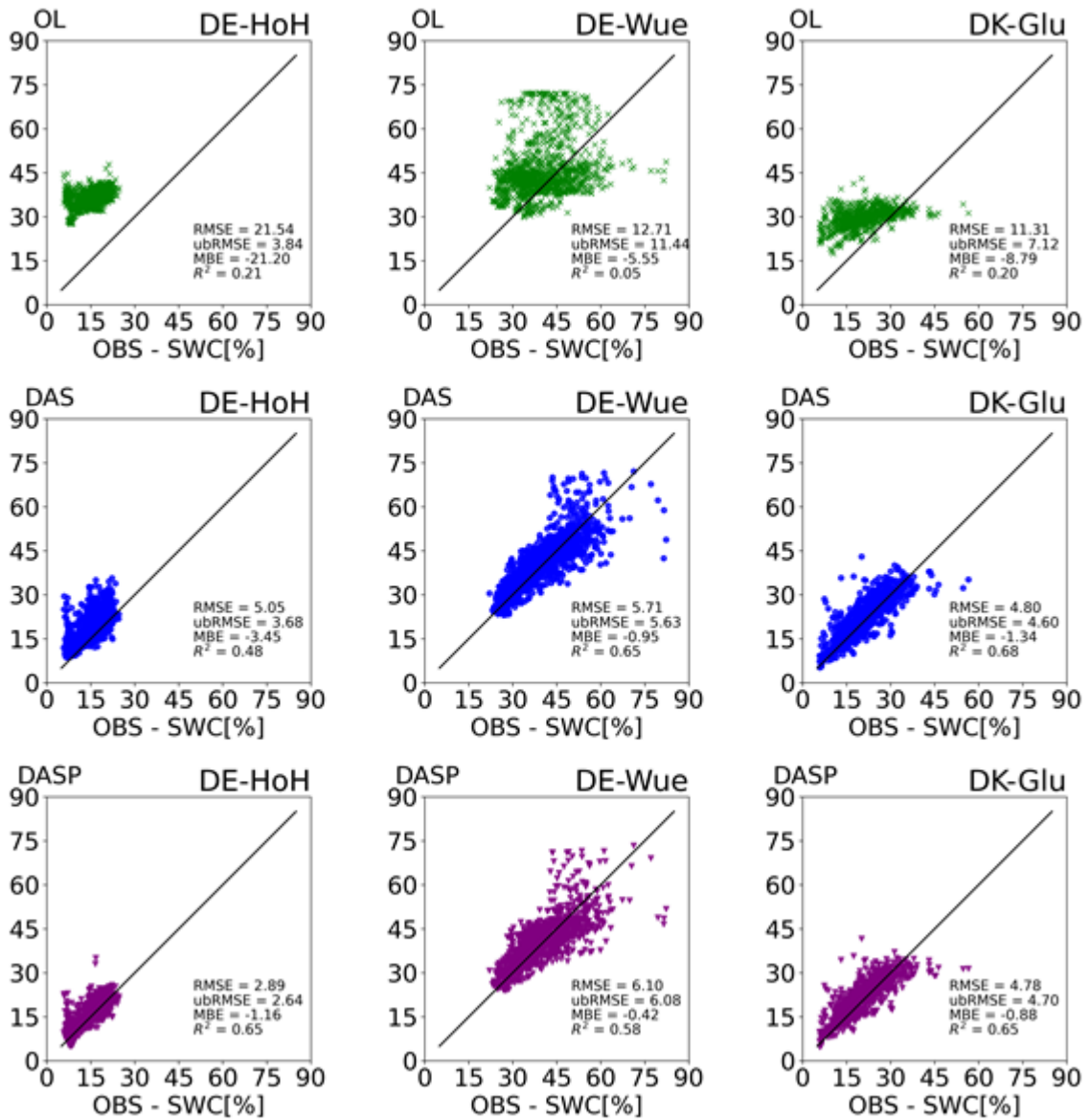


Figure 4: Scatter plots of observed soil water content at three CRNS study sites (DE-HoH left column, DE-Wue middle column, DK-Glu right column) versus simulation results (OL results in the top row, DAS results in the middle row, and DASP results in the bottom row). The points represent daily averages for the days on which observation data are available.

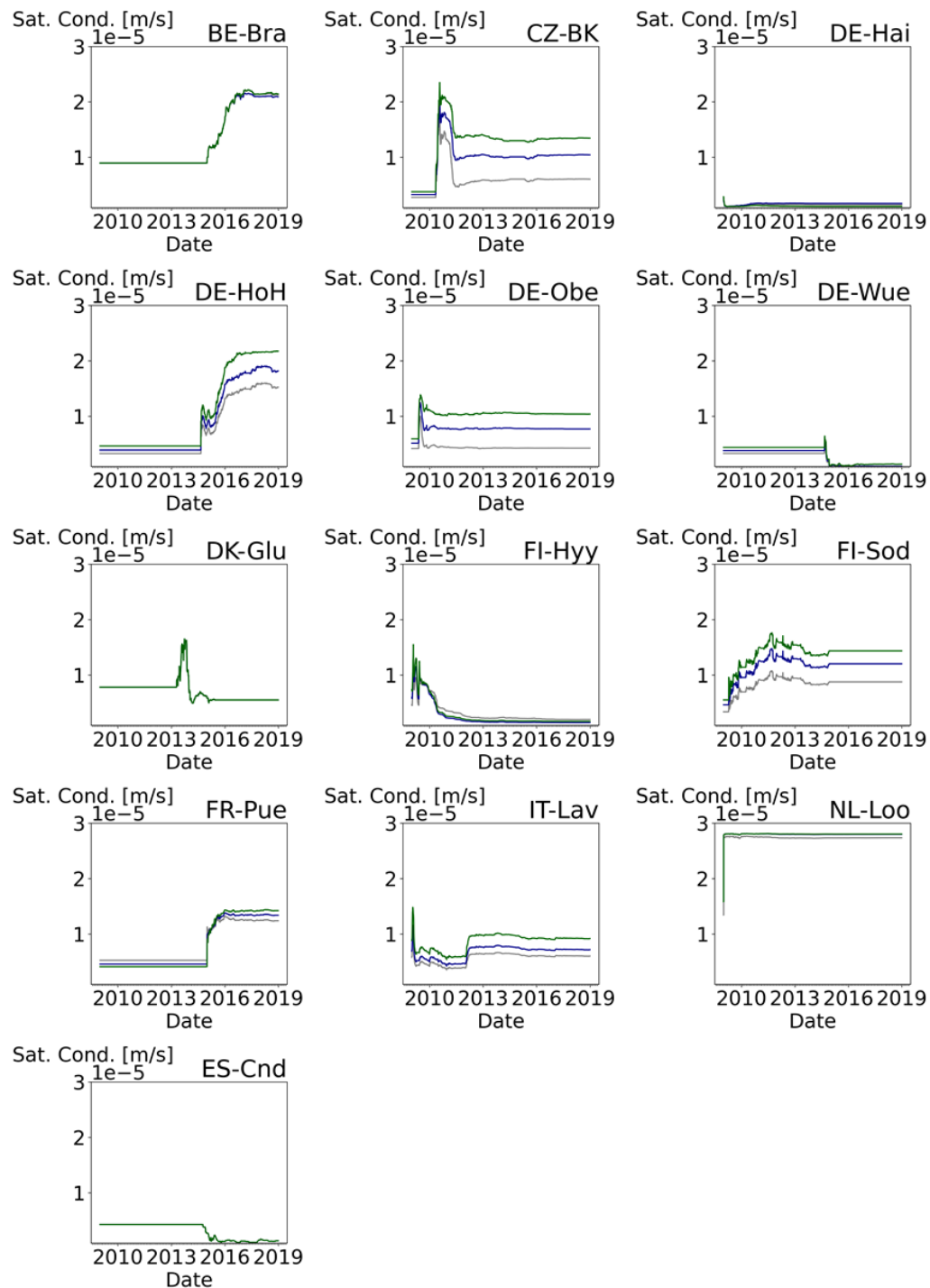
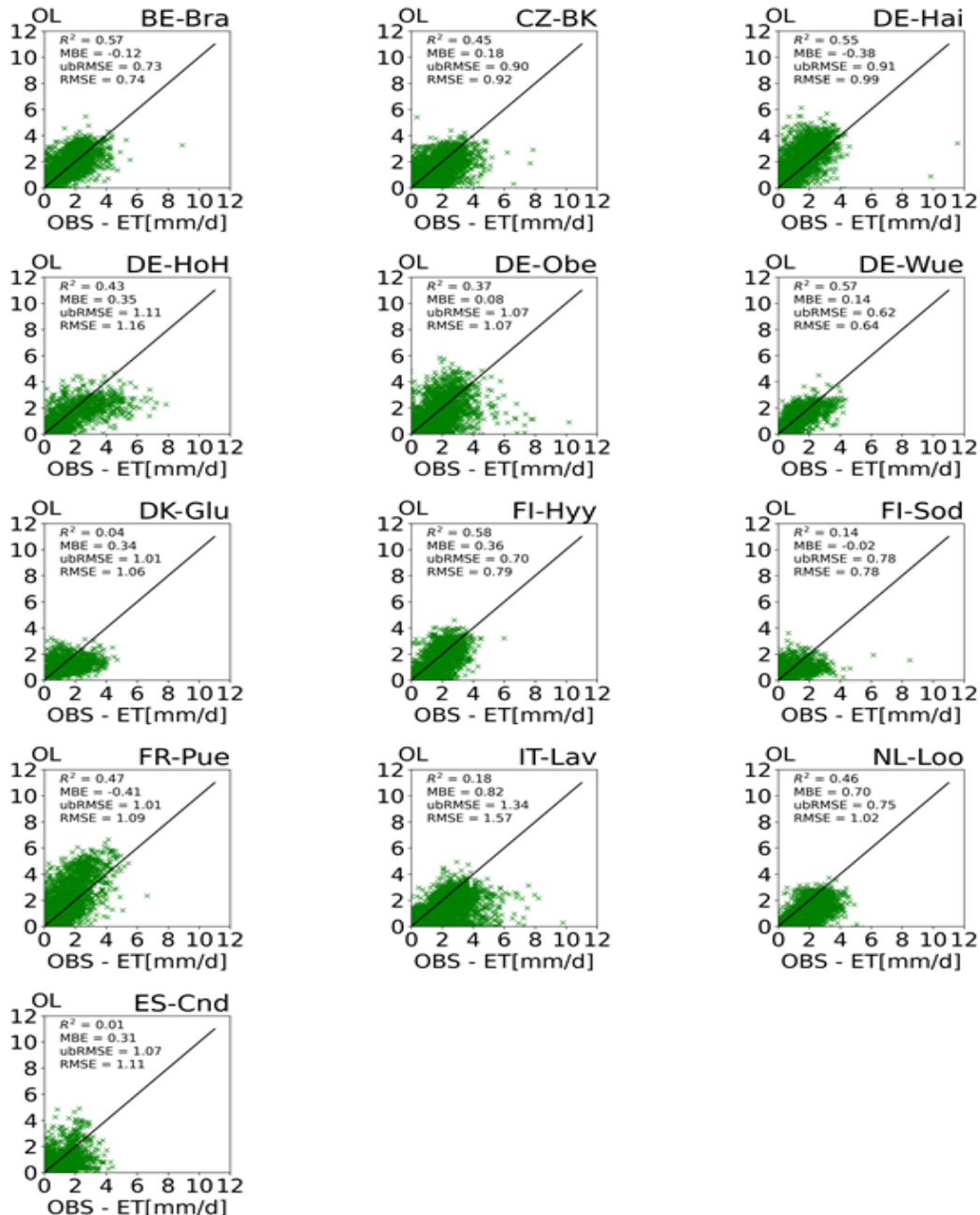


Figure 5: Time series of the saturated soil hydraulic conductivity for each site in the DASP simulation.

The grey line is the value at 5 cm depth, the blue line at 20 cm depth, and the green line at 50 cm depth.



The points represent daily averages for the days on which observation data are available.

For
12

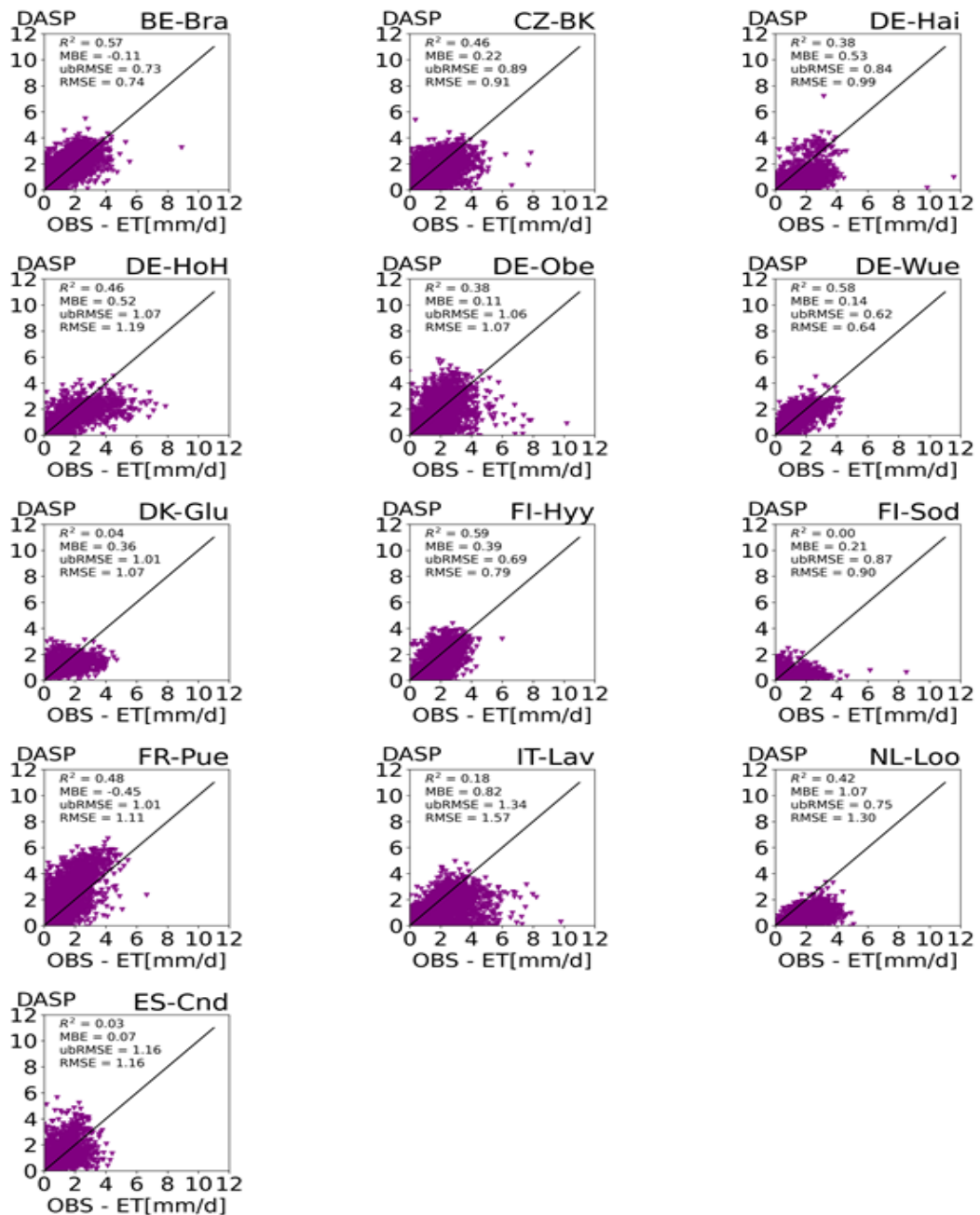


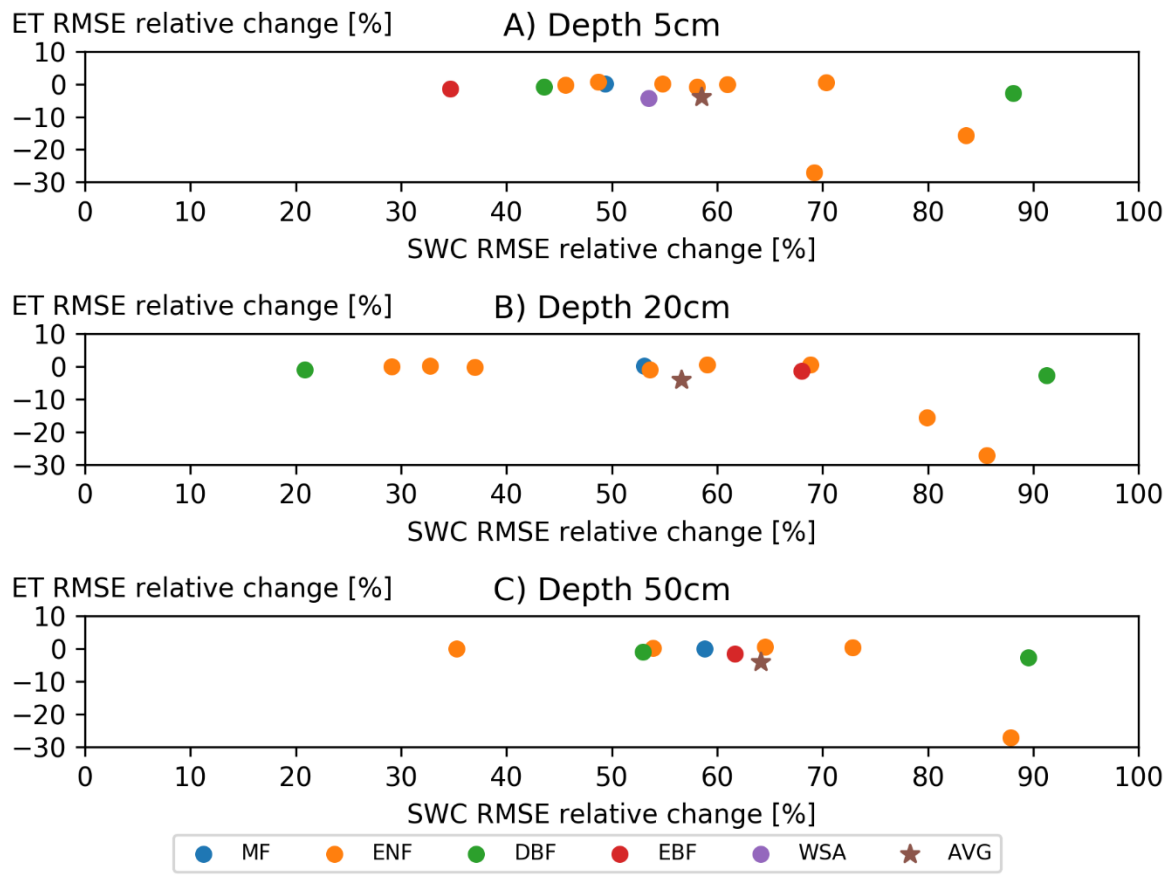
Figure 7: Scatter plots of observed evapotranspiration at thirteen study sites versus DASP simulation results. The points represent daily averages for the days on which observation data are available.

1690

For
Sch

For
Pt,

For
12



1700 **Figure 8:** Comparing the SWC and ET characterization for the OL and DASP simulations. Each point represents the overall average RMSE change for one site. The color of the points indicates the classification code for the different forest types (MF: mixed forest, ENF: evergreen needle leaf forest, DBF: deciduous broad leaf forest, EBF: evergreen broad leaf forest, AVG: average over all forest types).

For Sch
For Pt.
For 12
For Fet

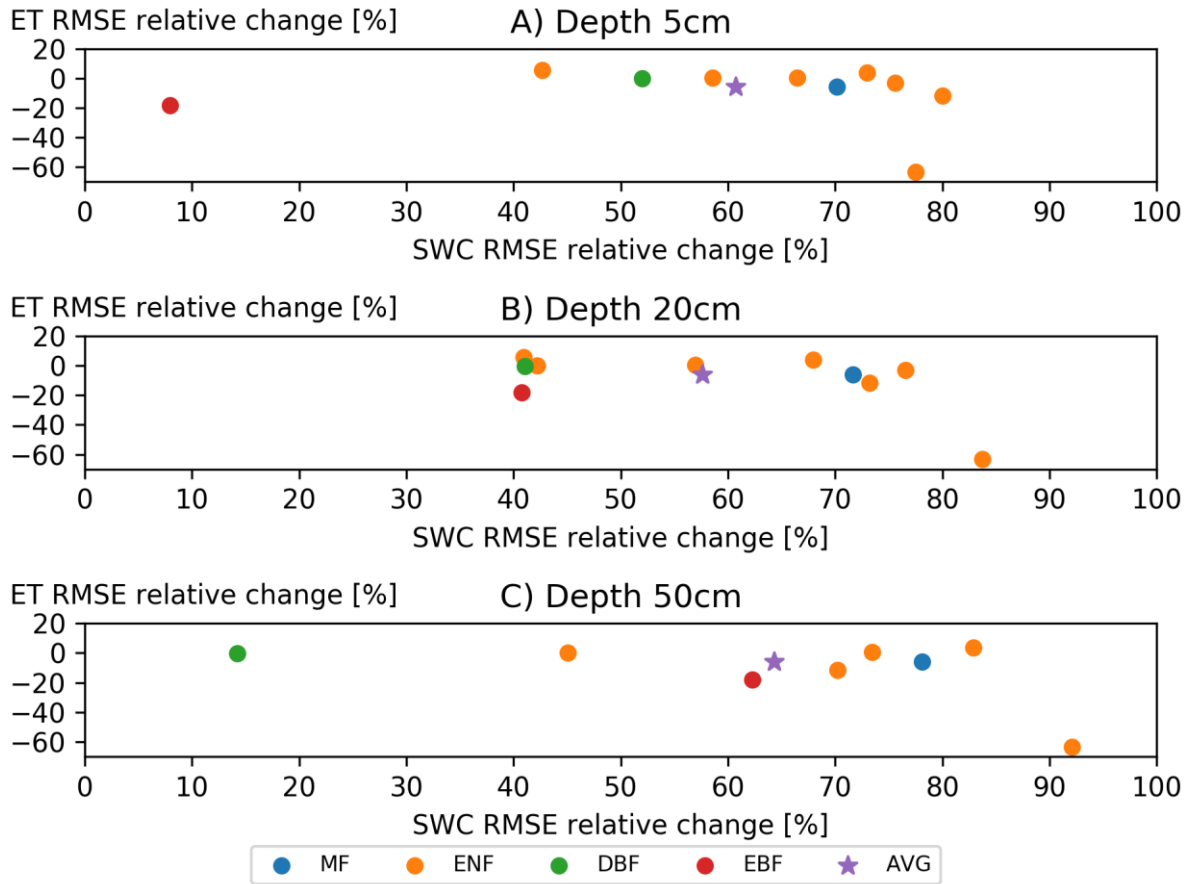
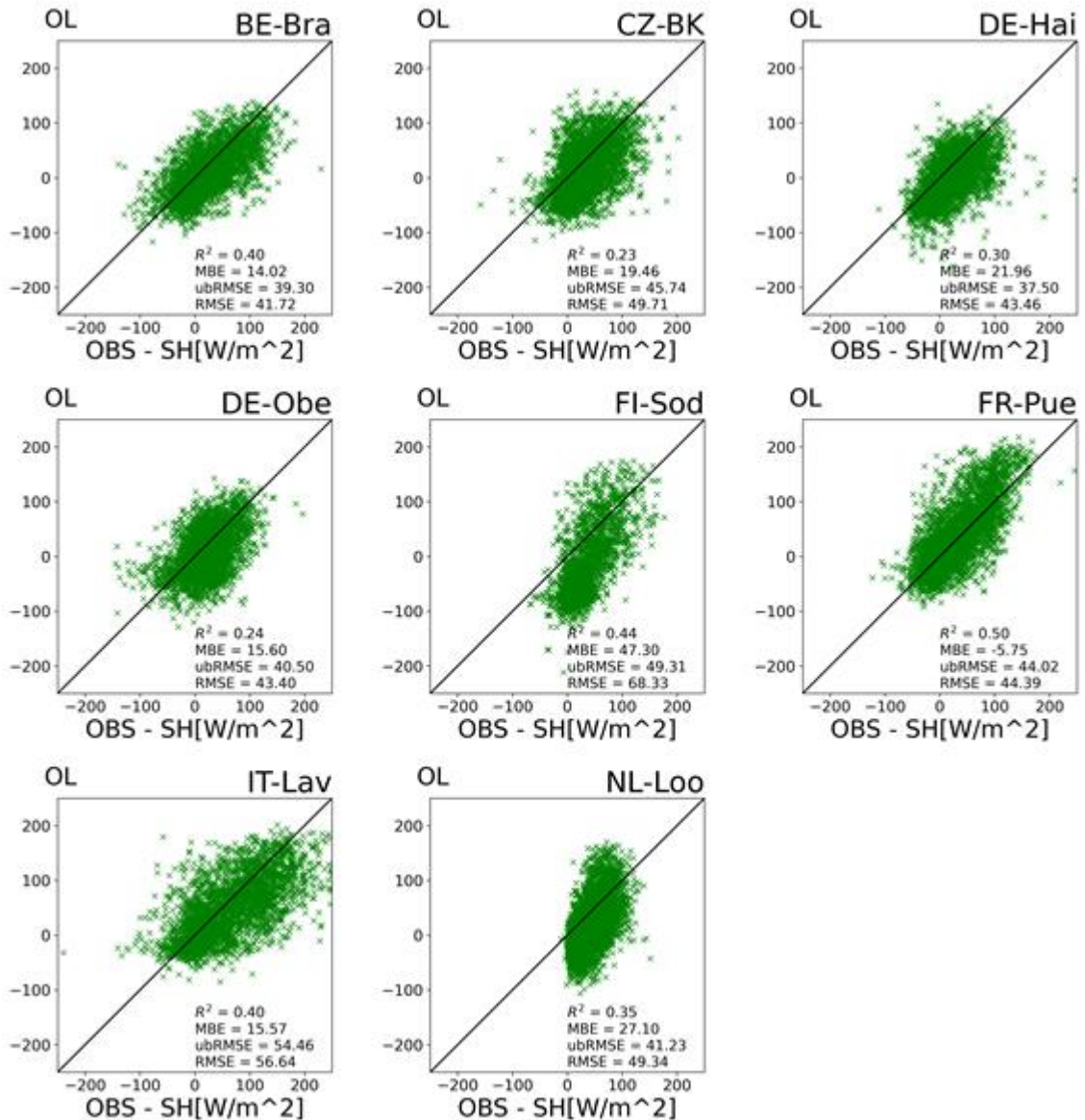


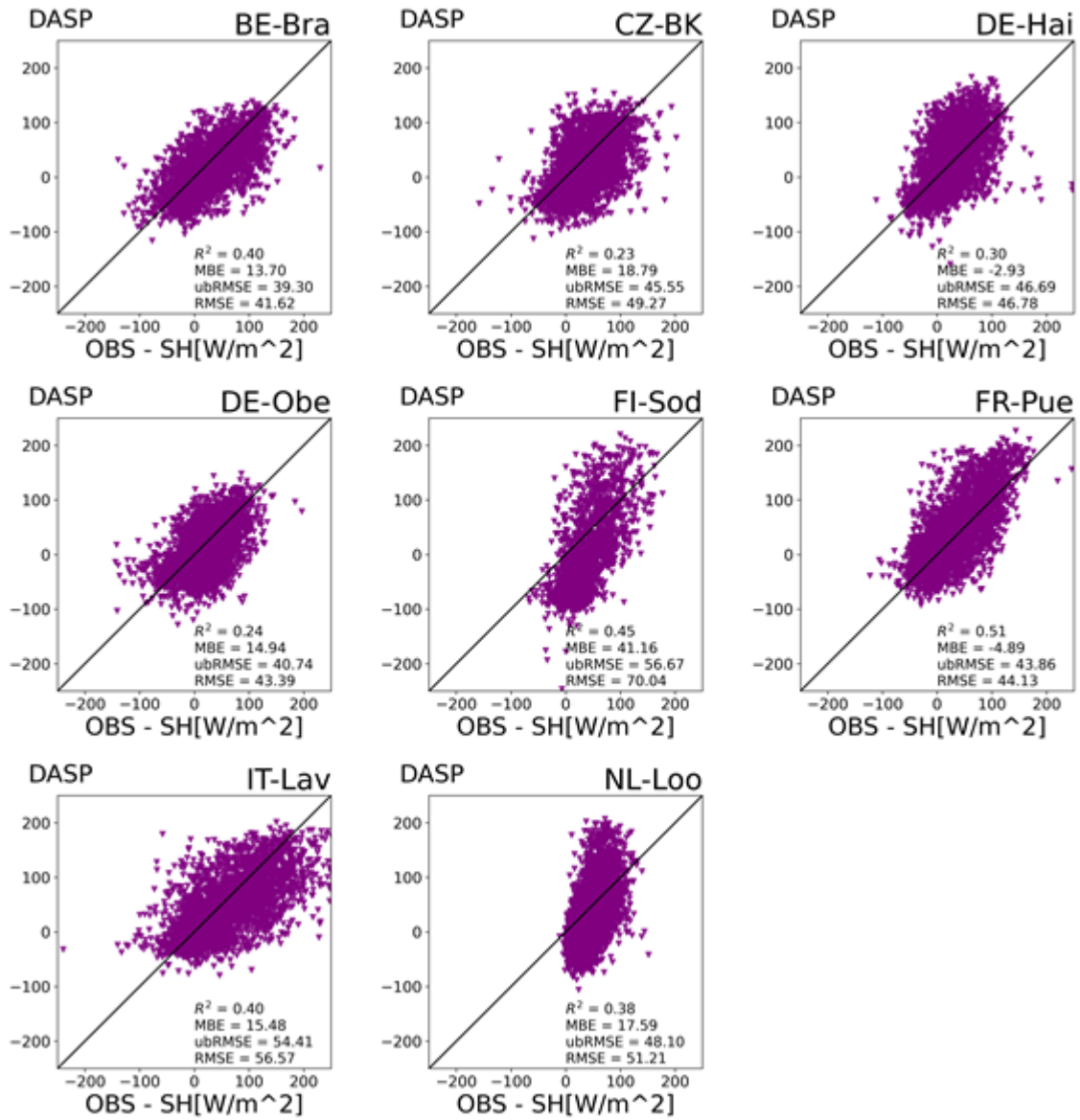
Figure 9: Comparing the SWC and ET characterization for the OL and DASP simulations using CLM5-SP. Each point represents the overall average RMSE change for one site. The color of the points indicate the forest type (MF: mixed forest, ENF: evergreen needle leaf forest, DBF: deciduous broad leaf forest, EBF: evergreen broad leaf forest, AVG: average over all forest types).



1715

Figure 10: Scatter plots of observed sensible heat flux at eight study sites versus OL simulation results. The points represent daily averages for the days on which observation data are available.

For
Pt.,
For
Sch
For
12



1725

Figure 11: Scatter plots of observed sensible heat flux at eight study sites versus DASP simulation results. The points represent daily averages for the days on which observation data are available.

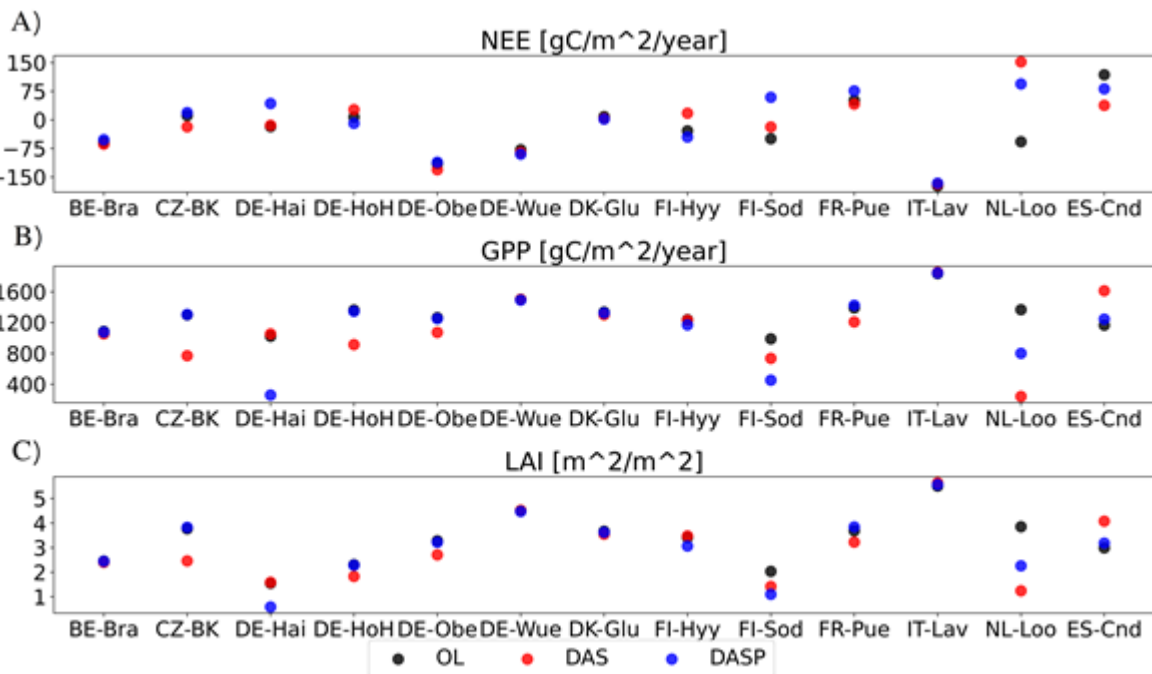


Figure 12: Open loop (OL) and assimilation scenario (DAS and DASP) yearly averages of A) net ecosystem exchange (NEE), B) gross primary production (GPP), and C) leaf area index (LAI) for all selected sites.

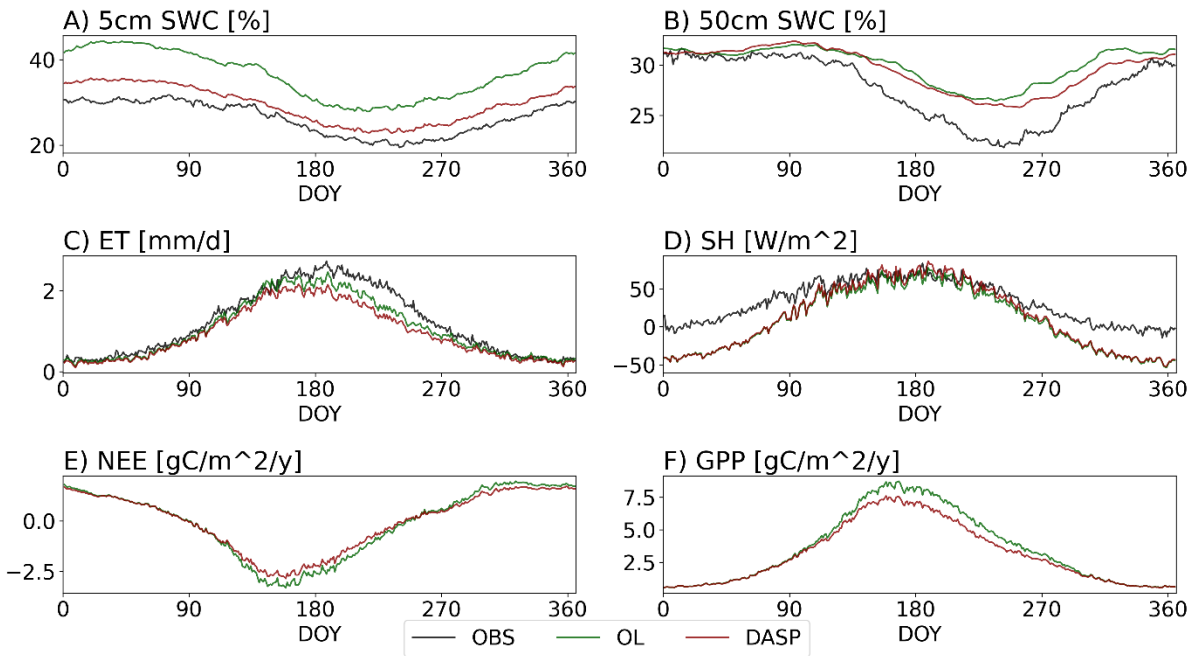


Figure 13: Seasonality of observed (OBS) and simulated (OL and DASP) states and fluxes based on daily averages from all years (2009 to 2018) and all sites: A) soil water content (SWC) at 5 cm depth, B) SWC at 50 cm depth, C) evapotranspiration (ET), D) sensible heat flux (SH), E) net ecosystem exchange (NEE), and F) gross primary production (GPP).

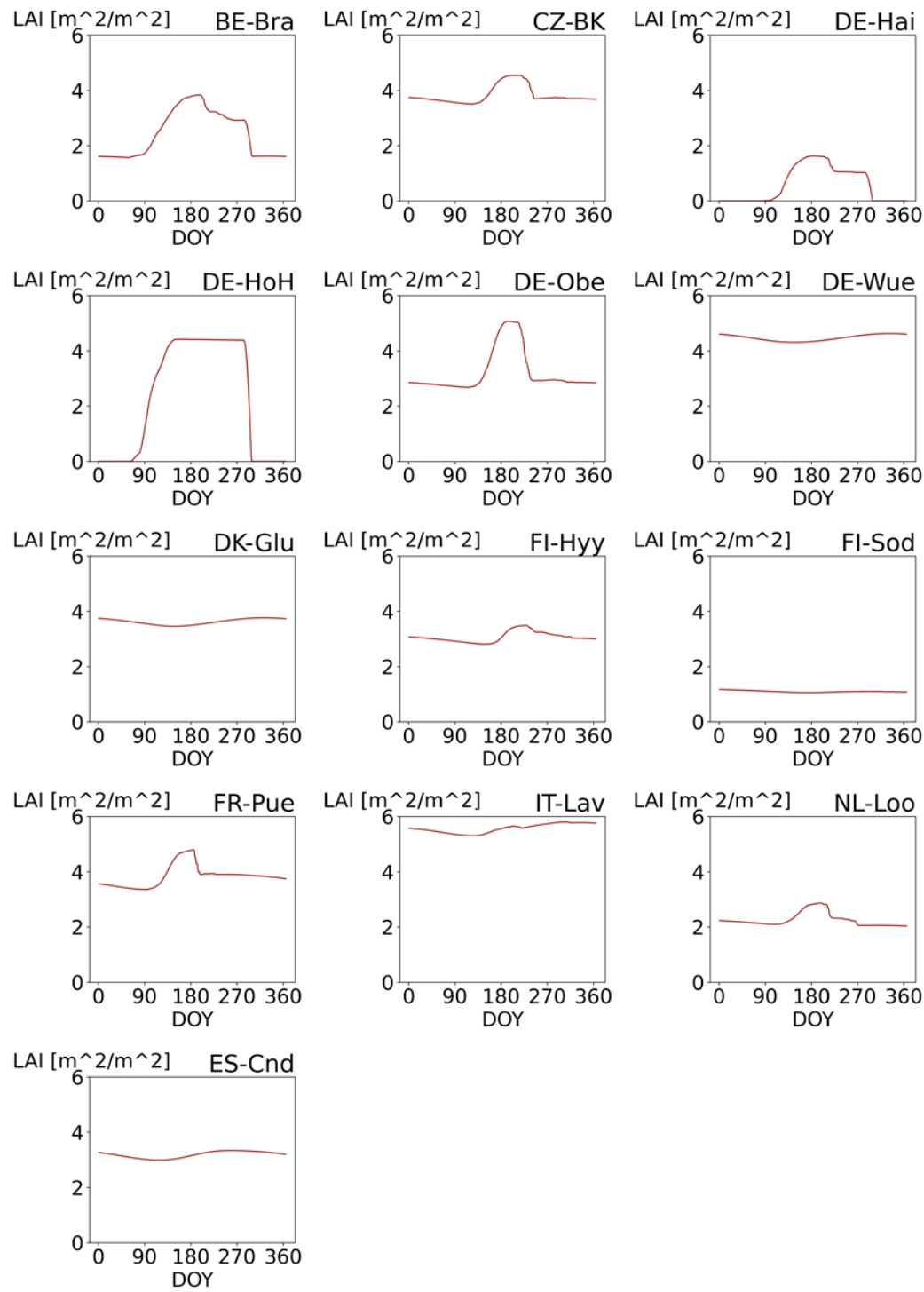


Figure 14: Seasonality of simulated (DASP) Leaf Area Index for each of the sites.

A. Additional figures

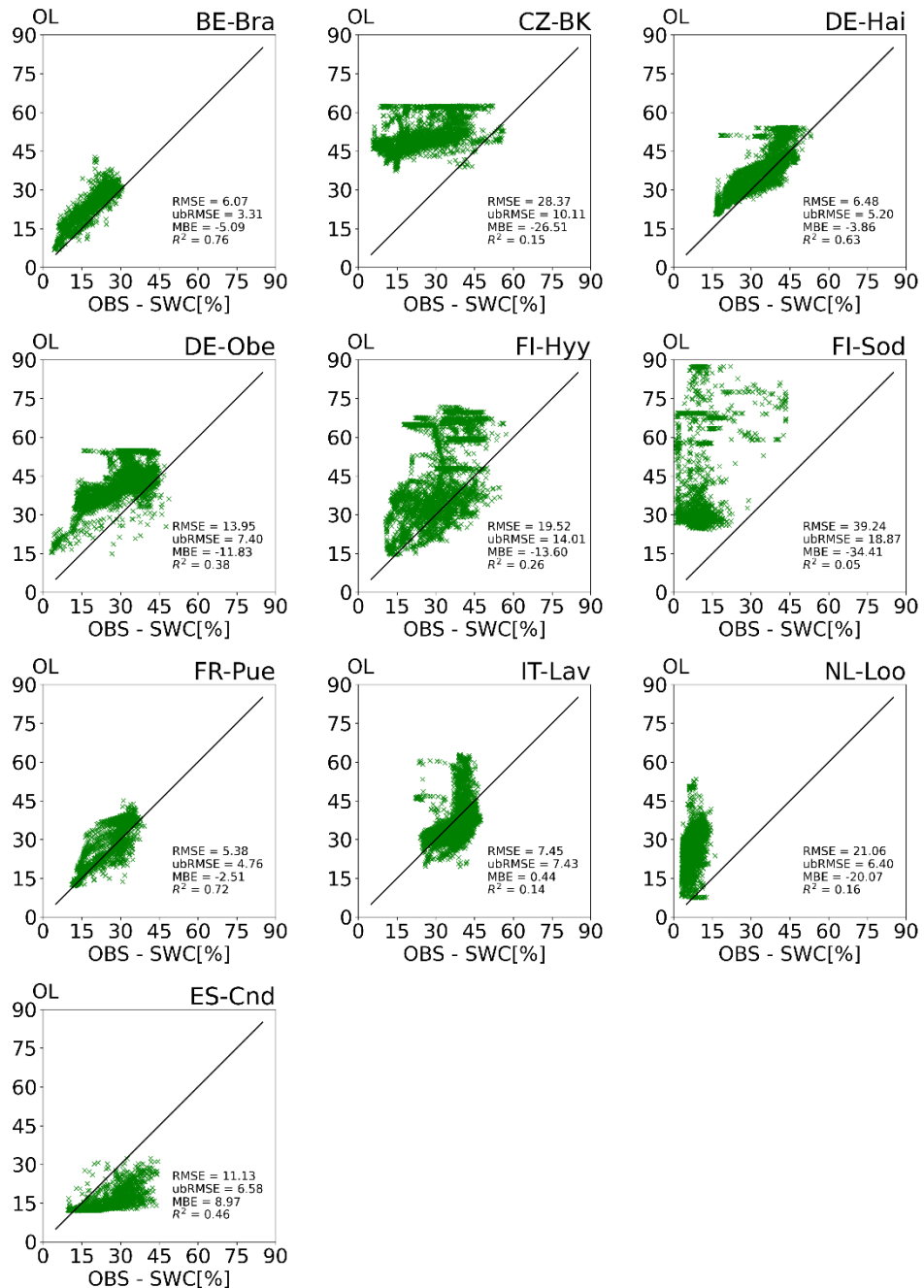


Figure A1: Scatter plots of observed soil water content at ten study sites versus OL simulation results at 5 cm depth. The points represent daily averages for the days on which observation data are available.

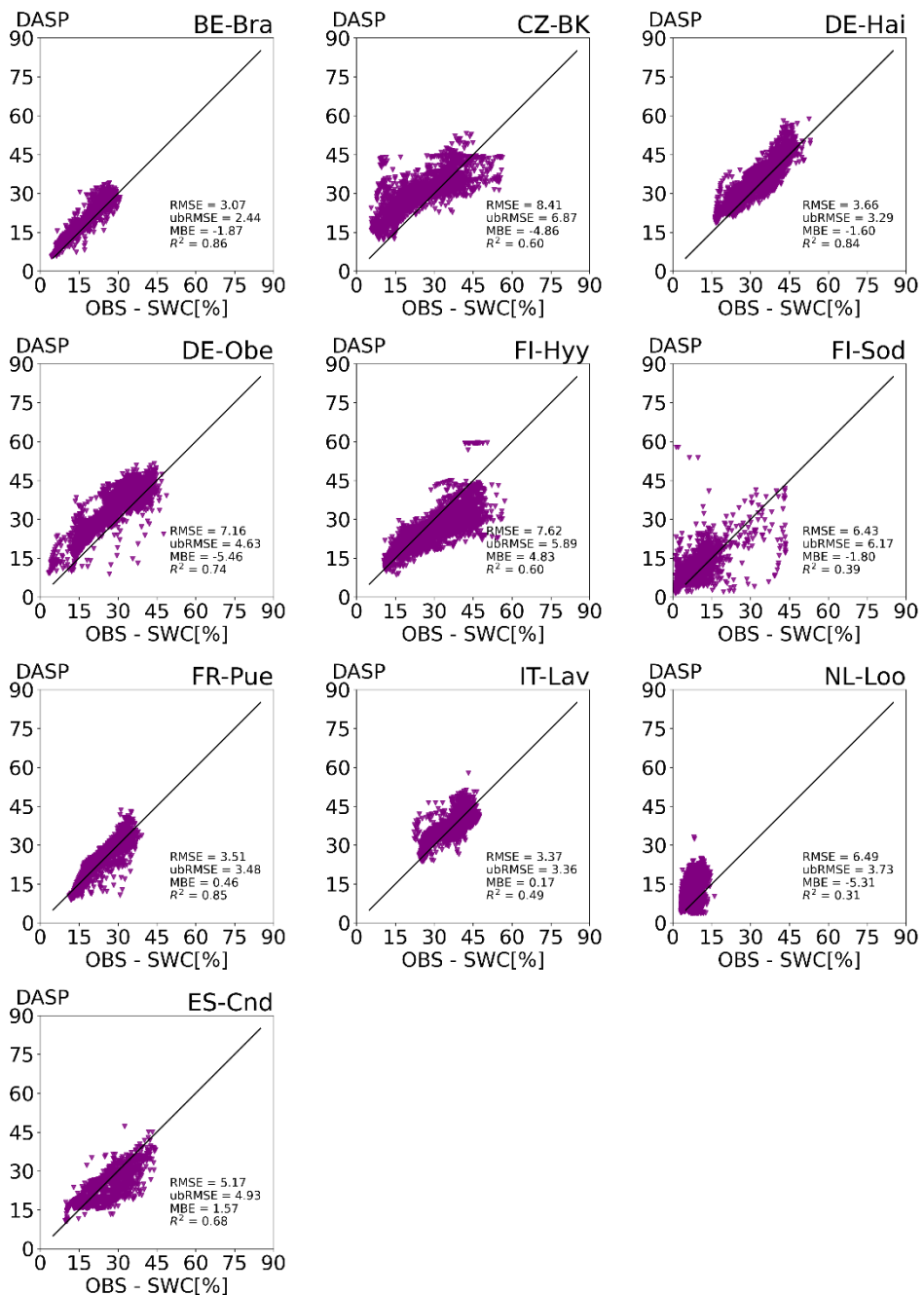
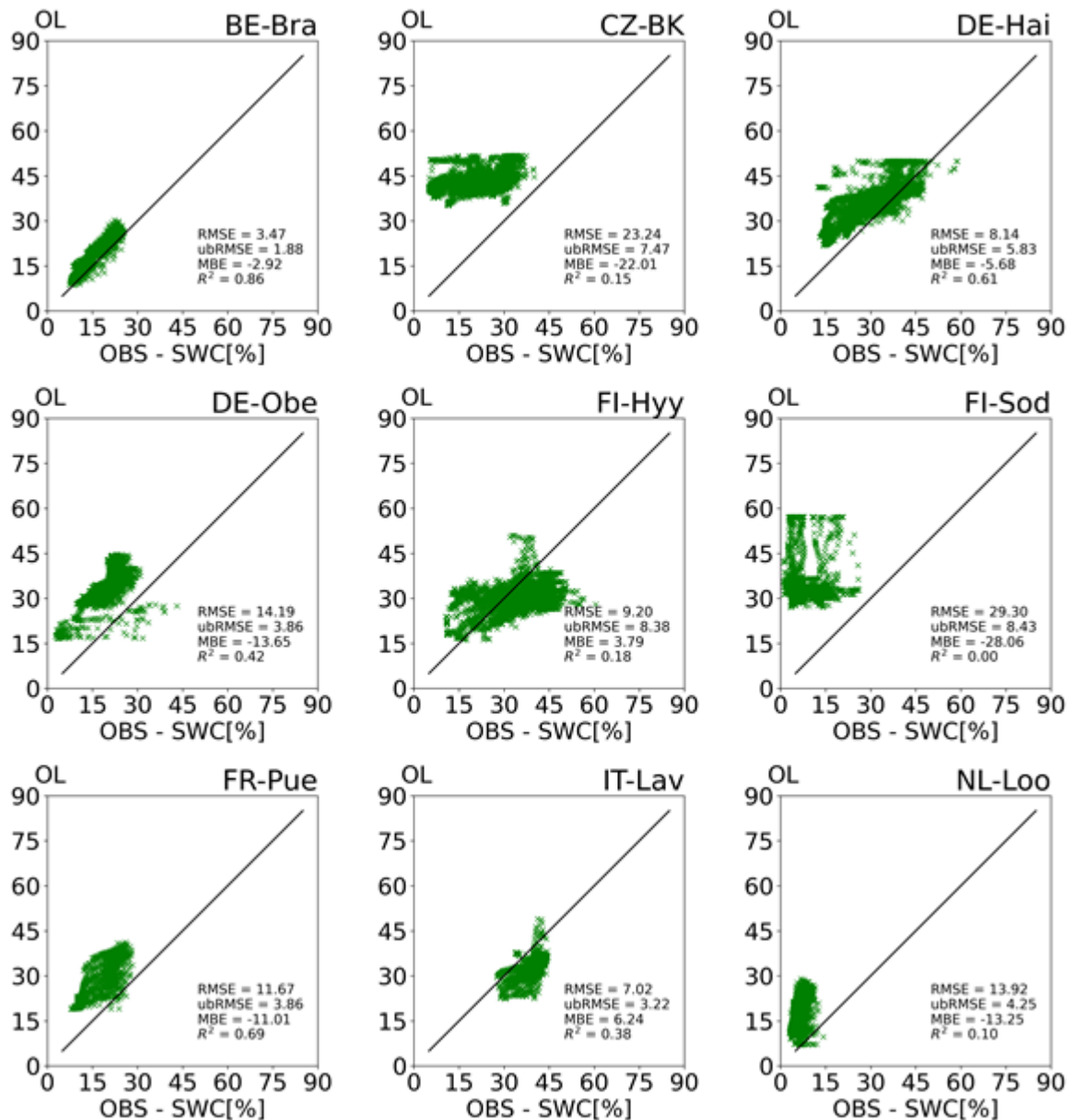


Figure A2: Scatter plots of observed soil water content at ten study sites versus DASP simulation results.

at 5 cm depth. The points represent daily averages for the days on which observation data are available.



1760

Figure A3 : Scatter plots of observed soil water content at ten study sites versus OL simulation results at 20 cm depth. The points represent daily averages for the days on which observation data are available.

For
12

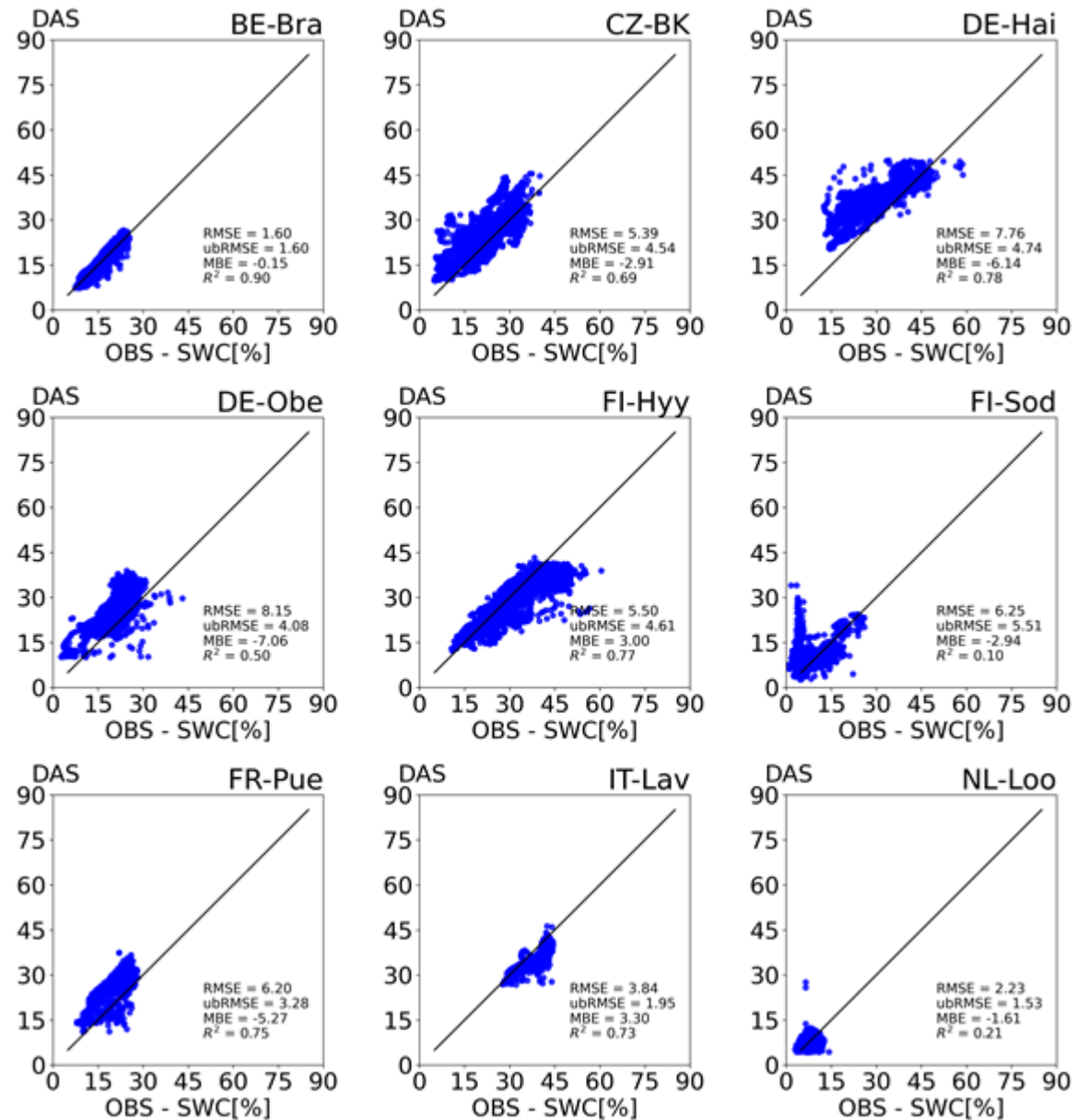


Figure A4 : Scatter plots of observed soil water content at ten study sites versus DAS simulation results at 20 cm depth. The points represent daily averages for the days on which observation data are available.

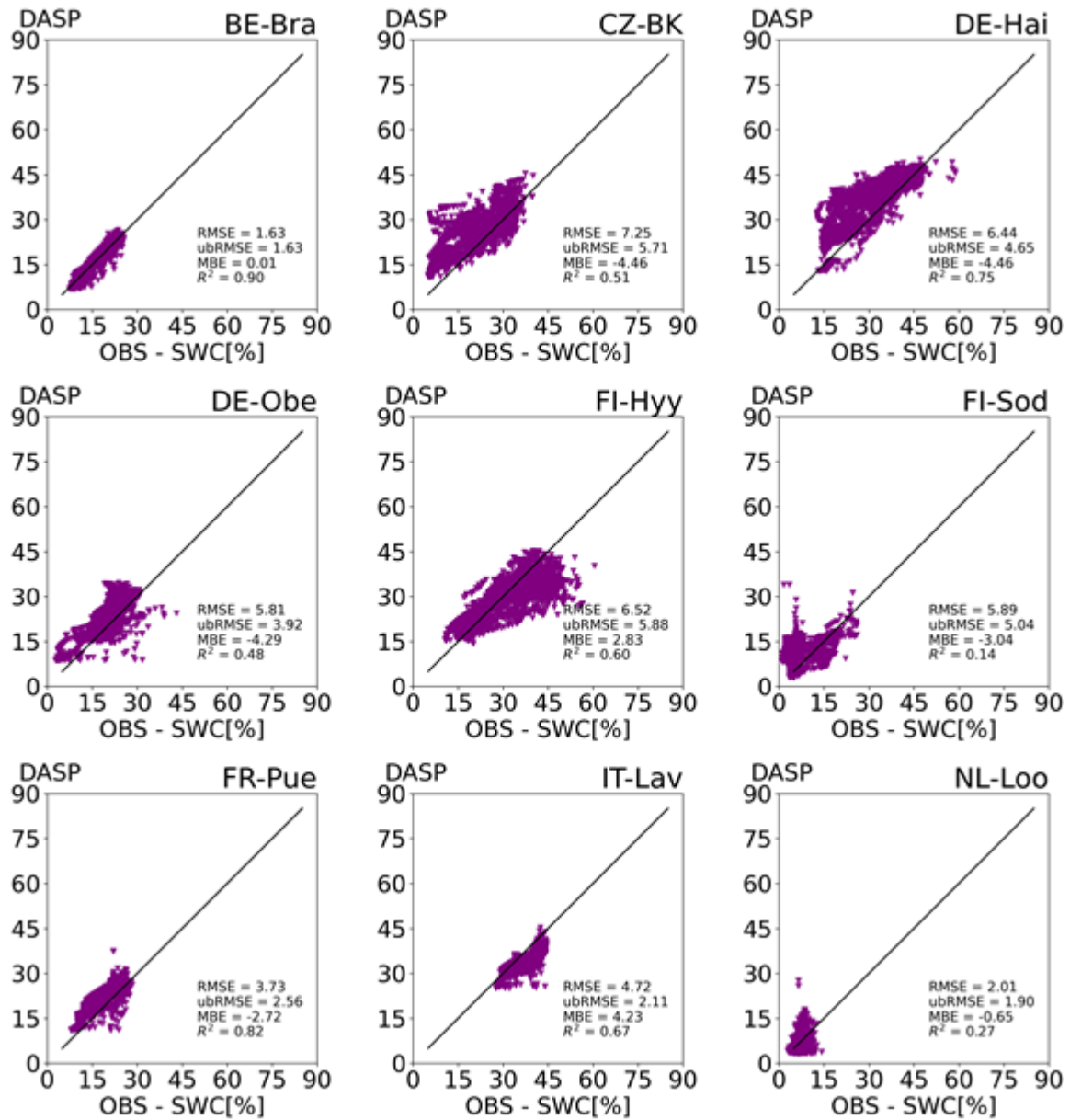
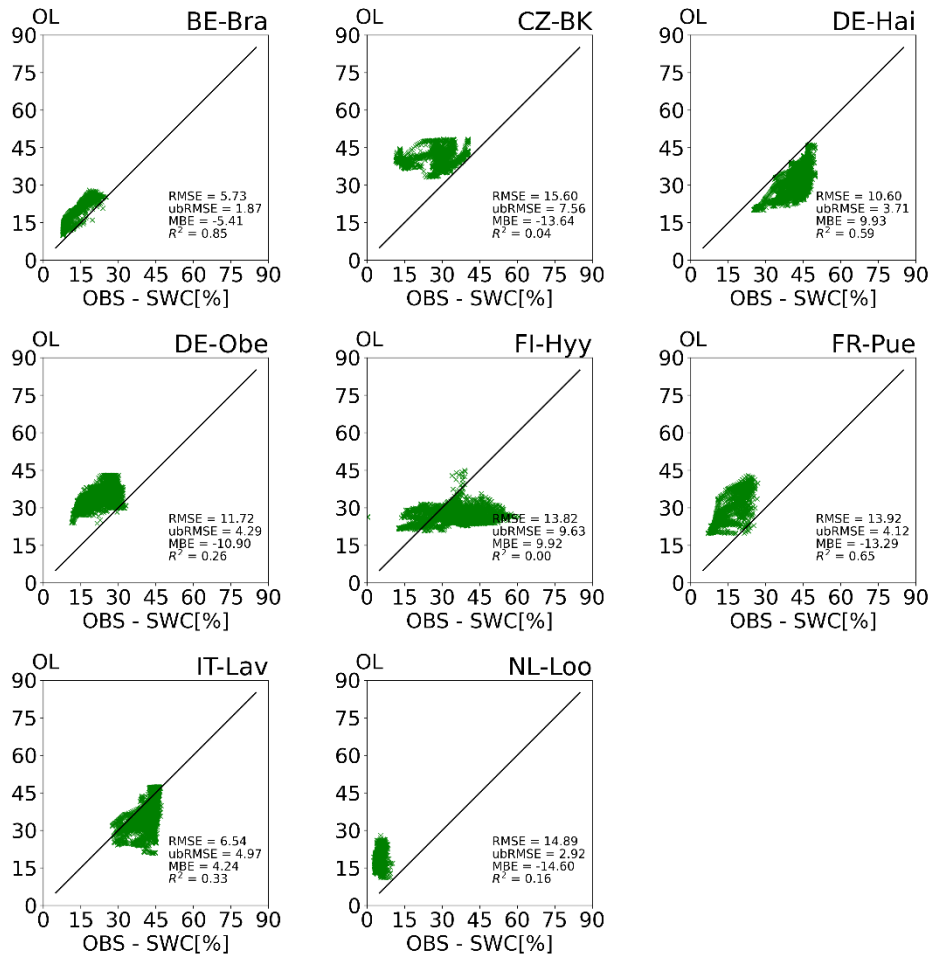


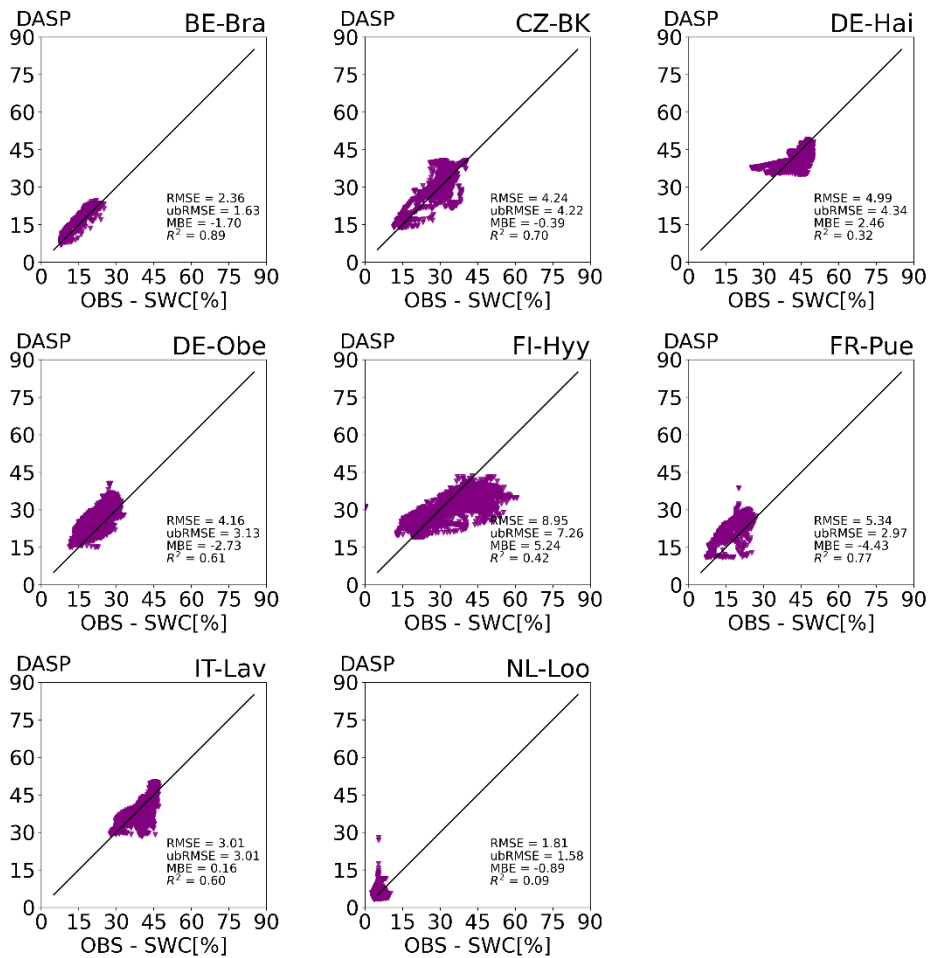
Figure A5 : Scatter plots of observed soil water content at ten study sites versus DASP simulation results at 20 cm depth. The points represent daily averages for the days on which observation data are available.



1775

Figure A6: Scatter plots of observed soil water content at eight study sites versus OL simulation results at 50 cm depth. The points represent daily averages for the days on which observation data are available.

For Sch
For 12
For Sch



1780

Figure A7: Scatter plots of observed soil water content at eight study sites versus DASP simulation results at 50 cm depth. The points represent daily averages for the days on which observation data are available.

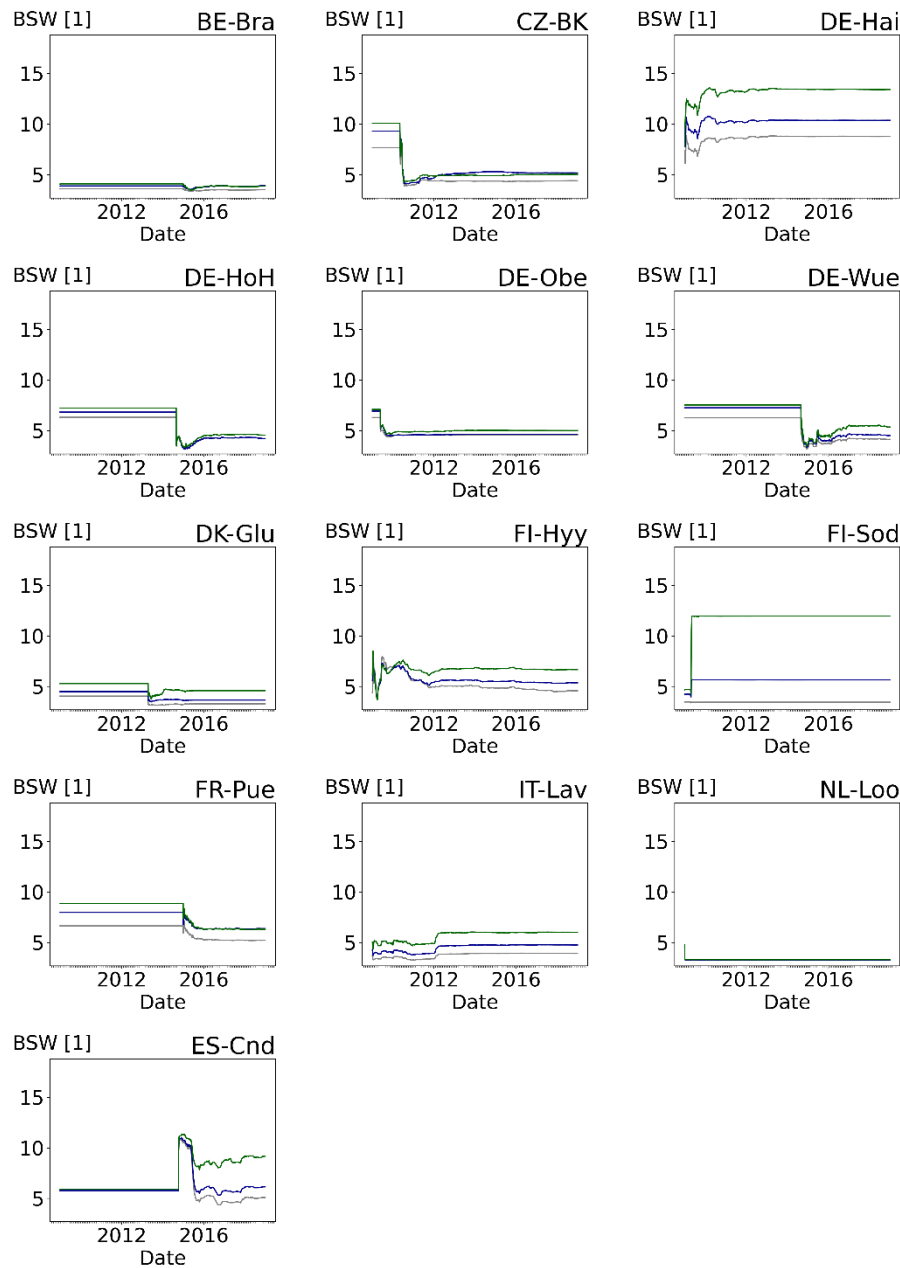


Figure A8: Time series for the Clapp-Hornberger shape parameter B (BSW) for each site in the DASP simulation. The grey line is the value at 5 cm depth, the blue line at 20cm depth, and the green line at 50cm depth.

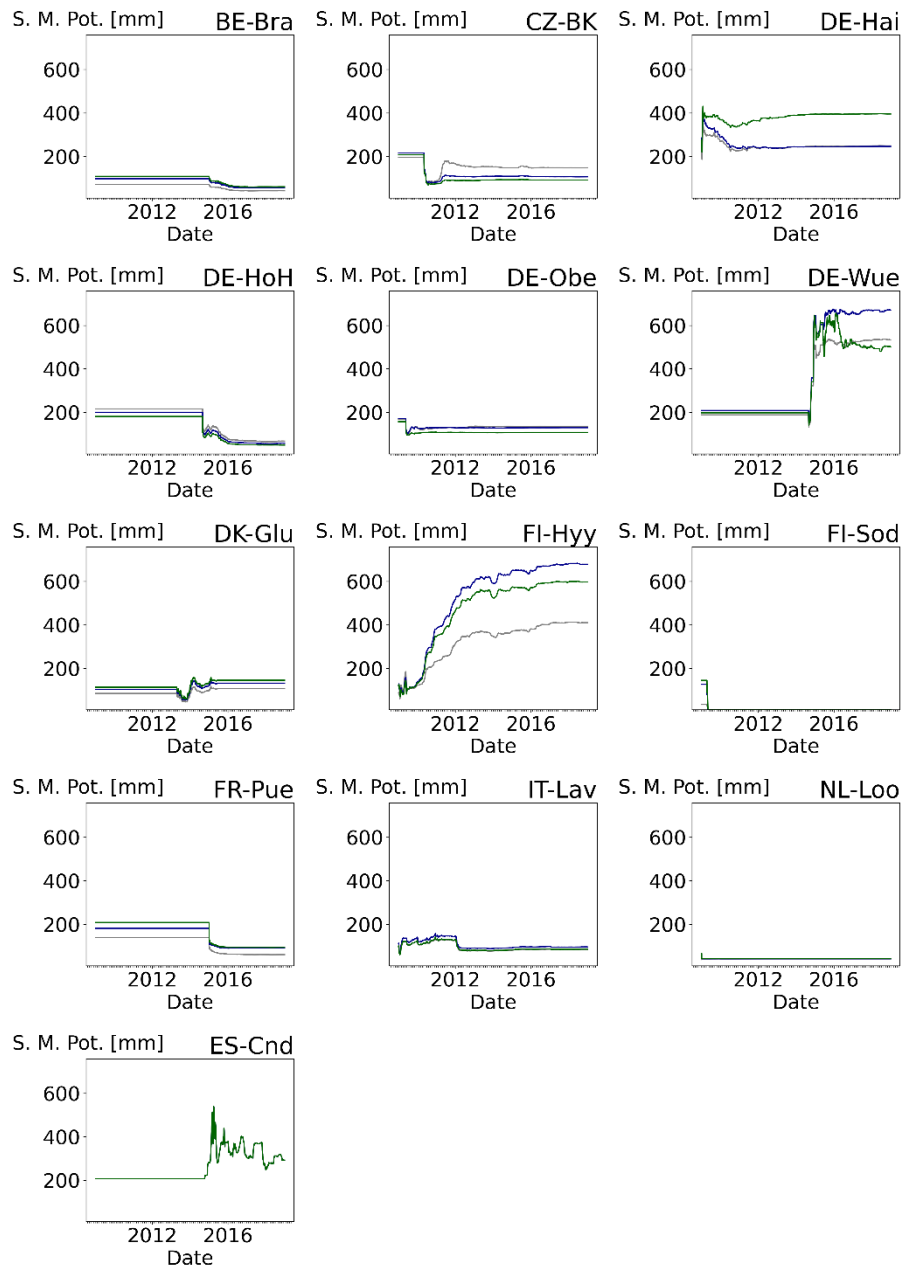
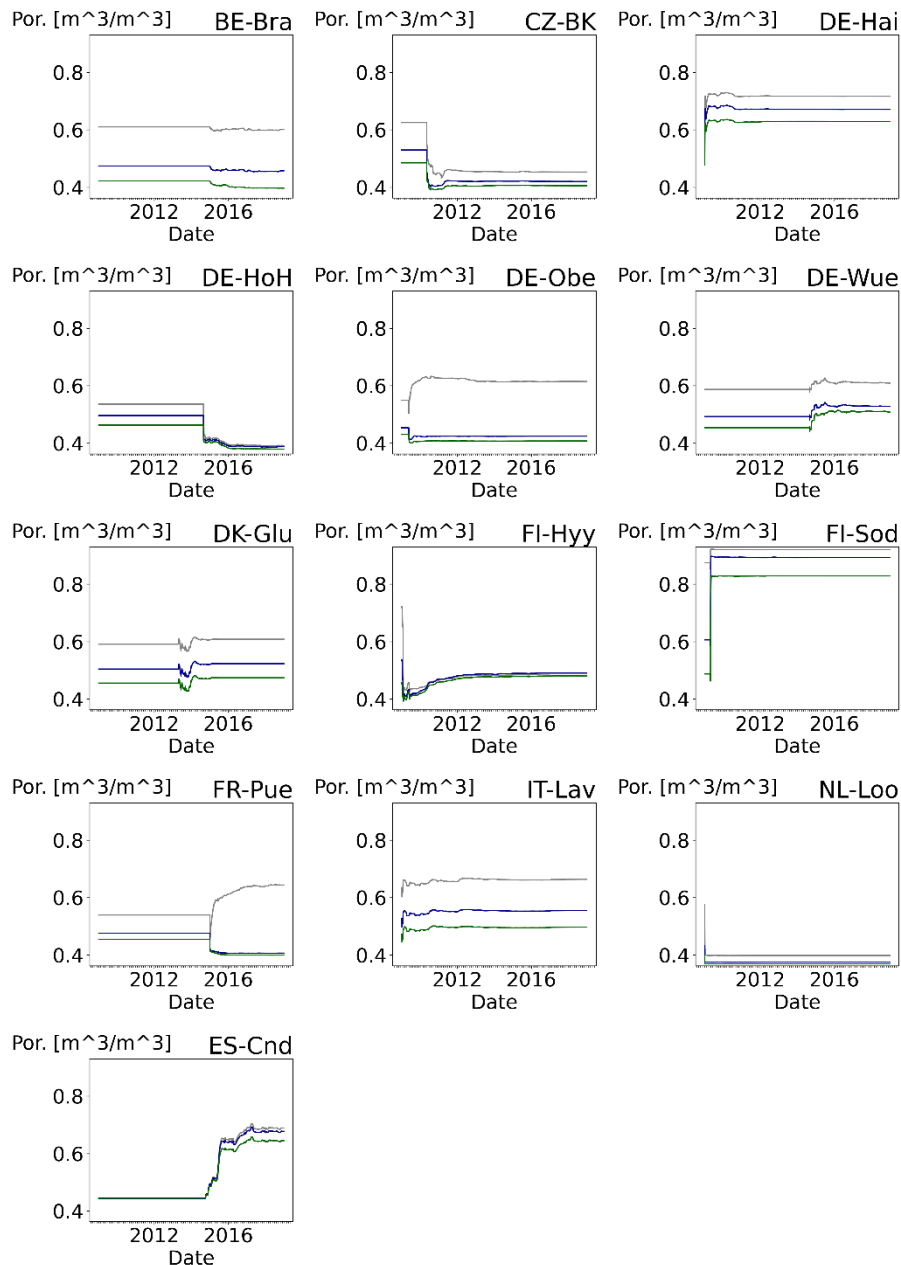


Figure A9: Time series for the soil matric potential for each site in the DASP simulation. The grey line is the value at 5 cm depth, the blue line at 20cm depth, and the green line at 50cm depth.



1790

Figure A10: Time series for the porosity for each site in the DASP simulation. The grey line is the value at 5 cm depth, the blue line at 20cm depth, and the green line at 50cm depth.

Code availability.

The code used in this study is available at <https://github.com/HPSCTerrSys/TSMP>.

Data availability.

1820 Data for the European FLUXNET sites is available at <http://www.europe-fluxdata.eu/>. Some additional data used in this study is from the eLTER data portal (<https://data.lter-europe.net/>) and ICOS data portal (<https://www.icos-cp.eu/>). The CRNS data is published in “Dataset of COSMOS-Europe: A European network of Cosmic-Ray Neutron Soil Moisture Sensors” available at <https://doi.org/10.34731/x9s3-kr48> (Bogena and Ney, 2021).

1825 **Competing interests.** The authors declare that they have no conflict of interest.

Author contribution.

1830 L.S. pre-processed the data, adjusted the code, performed the simulations, and prepared the manuscript. M.A. and S.A-B. provided data and contributed to the manuscript. H.B., H.J.H.F., and H.V. supervised the research, co-designed the experiments, and contributed to the manuscript.

Acknowledgements.

1835 The authors gratefully acknowledge the support by the project “LIFE RESILIENT FORESTS – Coupling water, fire and climate resilience with biomass production from forestry to adapt watersheds to climate change”. Additionally, the authors gratefully acknowledge the support by the Deutsche Forschungsgemeinschaft (DFG, German Research Foundation) – SFB 1502/1–2022 - Projekt-nummer: 450058266. Furthermore, the authors gratefully acknowledge the computing time granted through JARA on the supercomputer JURECA at Forschungszentrum Jülich. We are thankful for all the data provided by FLUXNET, LTER, ICOS, COSMOS-Europe projects and we thank the site PI and technical staff of the sites shown in this study.